

# Quantum Simulations for Extreme Ultraviolet Photolithography

Tyler D. Kharazi,<sup>1,2</sup> Stepan Fomichev,<sup>1</sup> Shu Kanno,<sup>3</sup> Takao Kobayashi,<sup>3</sup> Juan Miguel Arrazola,<sup>1</sup> Qi Gao,<sup>3</sup> and Torin F. Stetina<sup>1</sup>

<sup>1</sup>*Xanadu, Toronto, ON, M5G2C8, Canada*

<sup>2</sup>*Department of Chemistry, University of California, Berkeley, Berkeley, California 94720, USA*

<sup>3</sup>*Science & Innovation Center, Mitsubishi Chemical Corporation, 1000, Kamoshida-cho, Aoba-ku, Yokohama 227-8502, Japan*

Extreme Ultraviolet (EUV) lithography is the state-of-the-art process in semiconductor fabrication, yet its spatial resolution is fundamentally limited by the line edge roughness or “blur” originating from absorption of photons at 92 eV, which induce physical and chemical changes in the photoresist via excited state processes and electron cascades. Accurate modeling of these phenomena requires precise ab initio data for high-energy decay channels, specifically photoabsorption and photoelectron emission. These are computationally difficult for classical methods due to prohibitive scaling in simulating electron dynamics, or due to the inability to resolve the ionization continuum in an efficient manner. In this work, we present quantum simulation algorithms to compute these key observables. First, we introduce a coherent time-domain spectroscopy simulation algorithm optimized to resolve the photoabsorption cross-section at the 92 eV operating frequency. Second, we develop a first-quantized plane-wave simulation to compute the photoelectron kinetic energy spectrum, utilizing real-time dynamics and energy windowing to treat bound and delocalized scattering states on equal footing. Additionally, we provide logical resource estimations for a model photoresist monomer, 4-iodo-2-methylphenol (IMePh), and demonstrate that 92 eV absorption sensitivity can be resolved using roughly 200 logical qubits and  $10^9$  total non-Clifford gates per circuit with approximately  $10^3$  shots for the smallest non-trivial instance. The more sophisticated photoemission algorithm that models the continuum explicitly, incurs gate costs of  $\geq 10^{13}$  total non-Clifford gates per circuit,  $10^4$  shots, and requires on the order of a few thousand logical qubits. These results establish high-fidelity quantum simulations as a key component to parameterize the multi-scale macroscopic models required to overcome the electron blur bottleneck in semiconductor miniaturization, and provide a starting point for further algorithmic optimization.

## I. INTRODUCTION

Extreme Ultraviolet (EUV) photolithography underpins the manufacturing of next-generation semiconductor devices, yet further reducing the size of transistors is fundamentally constrained by line edge roughness and “blur” inherent to the EUV exposure mechanism. Unlike deep ultraviolet (DUV) lithography driven by direct photochemistry, EUV patterning relies on a multi-stage electronic cascade. The absorption of a 92 eV photon triggers an immediate attosecond-scale photoionization, followed by a relaxation phase spanning femtoseconds where Auger decay and inelastic scattering generate a shower of low-energy secondary electrons [1–3]. It is this secondary population, in addition to the primary photoelectron, that both significantly drive the chemical transformation of the photoresist. Since the spatial extent of this electron cascade competes with the intended nanometer feature sizes, the predictive design of photoresists requires accurate simulation of the high-energy decay channels, specifically photoabsorption and Auger electron emission, that define the initial conditions for this complex process over multiple scales; spatially, and temporally [4, 5].

The photoabsorption cross-section at the EUV operating energy (92 eV) serves as the primary metric for screening photoresist candidate materials. Since this absorption event initiates the secondary electron cascade essential for lithographic patterning, the ability to reliably rank molecules by their sensitivity is a critical engineering objective. However, effective screening is currently obstructed by the computational complexity of resolving the many high energy states required to describe 92 eV excitations, as well as the electron correlation present in said excited states, requiring treatment beyond density functional theory (DFT) in some materials [6]. While accurate results are theoretically possible via correlated wavefunction based methods given a sufficiently large diffuse basis beyond DFT, the classical cost of solving for the thousands of correlated interior eigenstates is prohibitive while attempting to retain control over the accuracy of the computed results. In this work, we present a modified quantum absorption spectroscopy simulation algorithm to directly estimate the dipole autocorrelation function at a specific frequency (targeting the frequency dependent response at 92 eV), enabling the efficient calculation of the absorption cross-section. This is

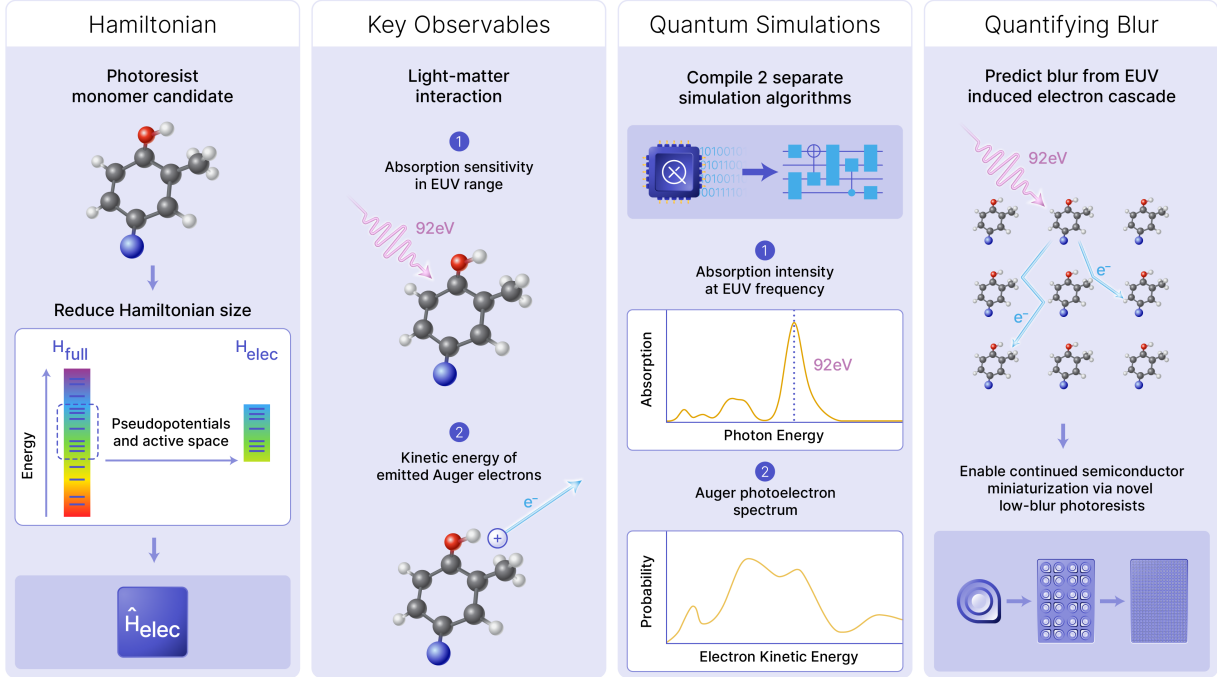


FIG. 1. Our proposed workflow for the *ab initio* design of low-blur EUV photoresists via quantum simulation. It connects atomic-scale electronic structure to macroscopic lithographic performance through four stages: (Hamiltonian) A candidate monomer, such as 4-iodo-2-methylphenol, is selected. Its full Hamiltonian ( $H_{full}$ ) is dimensionally reduced to an effective electronic Hamiltonian ( $H_{elec}$ ) utilizing pseudopotentials and/or active space selection to enable efficient simulation in a chosen basis and representation. (Key Observables) Two critical properties governing EUV lithography are targeted: the absorption sensitivity at the specific 92 eV operating frequency and the kinetic energy spectrum of secondary electrons generated via Auger decay. (Quantum Simulations) Two distinct quantum algorithmic primitives are compiled: a coherent time-domain approach to estimate the dipole autocorrelation function for absorption sensitivity, and a real-time electronic dynamics simulation to resolve the kinetic energy distribution of electrons ejected into continuum states. (Quantifying Blur) These quantum observables parameterize the initial conditions of electron cascades in larger bulk materials, allowing for the computational predictions of stochastic "electron blur" which ideally enables the design of materials that support continued semiconductor miniaturization.

an extension to previous work targeting the simulation of the spectrum over multiple frequencies simultaneously [7, 8]. The details of our approach for this task are presented in Section III.

Next, accurately predicting the low-energy Auger electron kinetic energy spectrum is a prerequisite for parameterizing the multi-scale models used to design EUV photoresists [3, 9–11]. A large portion of the lithographic chemistry in these systems is driven primarily by the cascade of low-energy secondary electrons rather than the initial high-energy photoelectron. Consequently, the emitted electron yield and its kinetic energy distribution are key parameters for determining the “dose-to-clear” and ultimate resolution of the etched material. However, choosing materials that increase EUV absorption using heavy-atom substitutions, such as iodinated organic photoresist monomers like 4-Iodo-2-

methylphenol (IMePh), has shown that DFT based simulations are not able to accurately model this process [3]. Specifically, these methods failed to reproduce the intense low-kinetic-energy spectral features observed experimentally, which are explicitly identified as Auger electrons. In general, the key target observable is the kinetic energy spectrum of a photoemitted electron which could correspond to either photoionization or Auger decay processes. Even though the previously mentioned DFT method was not accurate, there are other classical approaches that attempt to incorporate electron correlation and continuum effects in the literature, such as Feshbach-Fano approaches [12–14], R-matrix theory [15–18], and explicit real-time Green’s function based methods [19, 20]. The first two methods rely on approximate treatments of the continuum states, and the explicit time evolution approaches are typically

constrained to small model systems or perturbative treatment of electron correlation due to the computational complexity of the full many-body dynamics.

This simulation gap, which hinders the accurate parameterization of larger multi-scale models, stems from multiple causes. First, standard electronic structure methods typically rely on spatially localized basis sets, typically Gaussian orbital bases, that cannot accurately describe high-energy resonances embedded in the ionization continuum [21–23]. While plane-wave bases can more naturally represent the continuum states, classically simulating this in a sufficiently large volume is computationally prohibitive. Second, Auger electrons emitted from the EUV excited system form much slower in time than direct photoexcitation or photoemission, as a real-time simulation approach must evolve the correlated many-electron system over the femtosecond scale to observe Auger decay. The detailed description of our work in this direction is detailed in Section IV

In this work, we present two quantum simulation algorithms that compute key observables used in models predicting EUV-induced blur in photoresists. A summary of the results and workflows presented in this paper is shown in Fig. 1. The first observable is the EUV absorption sensitivity, or more specifically, the photoabsorption cross-section at 92 eV. For this task, we present a novel optimization of standard quantum algorithms for computing electronic spectra. The second observable is the kinetic energy spectra of electrons ejected from the target monomer, also referred to as the photoelectron emission spectra, or Auger spectra. For simplicity, we will refer to this as the *photoemission spectra* as a shorthand from here on. For this task, we present a first-quantized quantum simulation approach to efficiently compute the Auger spectra while accurately treating bound and continuum effects on equal footing.

The paper is structured as follows. First, we provide a theoretical background for electronic structure and the Hamiltonian in Section II. Then, we provide a novel optimization of the quantum simulation algorithm for computing absorption spectra, based on a coherent time-domain representation tailored towards single frequency absorption sensitivity in Section III. Next, we detail a quantum algorithm for photoelectron emission and Auger decay using a first quantized approach in Section IV. Finally, we provide quantum resource estimates using the IMePh monomer as a model system in Section V for both of the presented quantum simulation algorithms, and summarize our results in the conclu-

sion, Section VI.

## II. THEORETICAL BACKGROUND

For all results introduced in this paper, we consider the electronic structure model for a system of  $\eta$  electrons and  $L$  nuclei under the Born-Oppenheimer approximation, where we have clamped nuclei treated as classical point charges,  $\zeta_l$ , fixed at positions  $\mathbf{R}_l \in \mathbb{R}^3$ . Due to the short timescales of initial EUV excitation and electronic dynamics, this is an accurate approximation due to the fact that the nuclei are approximately static. Additionally, unless otherwise noted, we assume usage of atomic units throughout this work,  $\hbar = 4\pi\epsilon_0 = e = m_e = 1$  where  $\epsilon_0$  is the permittivity of free space,  $e$  is the electron charge, and  $m_e$  is the electron mass.

The electronic Hamiltonian is given by the contribution of four terms, the kinetic energy  $T$ , electron-nuclear attraction  $U$ , and electron-electron repulsion  $V$ , with a constant factor shift from the classical nuclear-nuclear repulsion energy,  $V_{nuc}$ , detailed below. The definition of the Hamiltonian is then

$$H = \sum_i^\eta \frac{\nabla_i^2}{2} + \sum_l^L \sum_i^\eta \frac{-\zeta_l}{|\mathbf{R}_l - \mathbf{r}_i|} + \frac{1}{2} \sum_{i,j}^\eta \frac{1}{|\mathbf{r}_i - \mathbf{r}_j|} + V_{nuc}, \quad (1)$$

where  $\nabla_i^2$  is the spatial Laplacian for particle  $i$ , and  $\mathbf{r}_i \in \mathbb{R}^3$  is the position of particle  $i$ .

While the Hamiltonian in Eq. (1) is the general *ab initio* model of non-relativistic electronic structure theory agnostic to a given basis, the distinct physics of photoabsorption and Auger decay use different assumptions and restrictions on the choice of an explicit basis. For the initial photoabsorption event, in which we target transitions between localized bound and Rydberg type states, we employ a compact second-quantized formulation (Section III) that efficiently captures electron correlation within a chemically relevant active space. Conversely, the subsequent Auger decay involves the ejection of electrons into high-energy scattering states, a process ill-suited for standard localized Gaussian basis sets, often found in quantum chemistry calculations. To rigorously model this continuum dynamics, we use a first-quantized plane-wave basis representation (Section IV) that naturally supports delocalized electronic wavefunctions, but typically requires a much larger basis to represent the physics accurately.

### III. PHOTORESIST SENSITIVITY

#### A. Background

In the first step of the EUV lithographic process, a focused light source at 92 eV is applied to the photoresist material. Provided that the photoresist has a significant absorption cross section at this excitation frequency, some of the incident light will be absorbed, leading to photoexcitation and potentially ionization of a relatively tightly bound, semi-core electrons, similar to X-ray absorption-like excitations. This absorption cross-section directly determines the key performance metric of the photoresist, its so-called *sensitivity*: any material candidate whose absorption cross-section is too low will not be an effective photoresist material for use in the photolithography process. This requirement then directly translates into one of our two key material design tasks: using a quantum simulation algorithm, calculate the EUV absorption cross-section at 92 eV, to determine whether the material candidate passes the EUV sensitivity threshold.

While EUV light is high-energy, it is still well described within the dipole approximation. This means we can reliably treat the photoexcitation in the semi-classical picture, where the incoming photon is treated as a classical perturbing electric field, while electrons in the photoresist are treated quantum mechanically.

Much as in the case of X-ray or ultraviolet-visible range absorption spectroscopy, the EUV absorption cross-section may be written using the Kramers-Heisenberg relation in atomic units as

$$\sigma_A(\omega) = \frac{4\pi}{3c}\omega \sum_{F \neq I} \sum_{\mu=x,y,z} \frac{|\langle \Psi_F | D_\mu | \Psi_I \rangle|^2 \gamma}{((E_F - E_I) - \omega)^2 + \gamma^2}, \quad (2)$$

where  $|\Psi_I\rangle, |\Psi_F\rangle$  are the initial and final many-body eigenstates of the photoresist molecule's Hamiltonian  $H$  with associated eigenvalues  $E_I, E_F$ , and  $\omega$  is the frequency of incoming radiation,  $c$  is the speed of light,  $\mu$  runs over the three Cartesian directions of the electric dipole operator  $D_\mu$ , and  $\gamma$  is the absorption line broadening.

For the purpose of quantum simulation, we reformulate this observable in terms of the imaginary part of the following Green's function

$$\mathcal{G}_\mu(\omega) = \langle \Psi_I | D_\mu \frac{1}{H - E_I - \omega + i\gamma} D_\mu | \Psi_I \rangle. \quad (3)$$

By substituting the resolution of identity between the Hamiltonian resolvent  $(H - E_I - \omega + i\gamma)^{-1}$  and

the dipole operator  $D_\mu$  and then taking the imaginary part, we can readily recover Eq. (2), up to multiplication by scalars. The photoresist Hamiltonian entering this definition may be represented either in first or second quantization: in this section, we find it convenient to express is in the latter form, namely

$$H_{SQ} = E + \sum_{p,q=1}^N (p|\kappa|q) a_p^\dagger a_q + \frac{1}{2} \sum_{p,q,r,s=1}^N (pq|rs) a_p^\dagger a_q^\dagger a_r a_s, \quad (4)$$

where  $a_p^{(\dagger)}$  is the annihilation (creation) operator for spin-orbital  $p$ ,  $E$  is the energy offset,  $N$  is the number of spin-orbitals, and  $(p|\kappa|q)$  and  $(pq|rs)$  are the one- and two-electron integrals, respectively, defined in chemist notation as

$$(pq|rs) \equiv \iint_{\mathbb{R}^6} d\mathbf{r}_1 d\mathbf{r}_2 \phi_p(\mathbf{r}_1) \phi_q(\mathbf{r}_1) \frac{1}{r_{12}} \phi_r(\mathbf{r}_2) \phi_s(\mathbf{r}_2) \quad (5)$$

$$(p|\kappa|q) \equiv \int_{\mathbb{R}^3} d\mathbf{r}_1 \phi_p(\mathbf{r}_1) \left( -\frac{1}{2} \nabla_{\mathbf{r}_1}^2 - \sum_A \frac{\zeta_A}{r_{1A}} \right) \phi_q(\mathbf{r}_1), \quad (6)$$

with  $\phi_p(\mathbf{r})$  being the  $p$ 'th spatial molecular orbital,  $\zeta_A$  being the atomic number of the  $A$ 'th atom, and  $r_{12} = |\mathbf{r}_1 - \mathbf{r}_2|$ ,  $r_{1A} = |\mathbf{r}_1 - \mathbf{r}_A|$  the distances between electronic positions  $\mathbf{r}_i$  and nuclei positions  $\mathbf{R}_A$ .

#### B. Coherent time-domain algorithm

Unlike in many prior works on spectroscopy, the specifics of the EUV application are such that rather than needing access to the entire spectrum, as in a fingerprinting application [7, 24, 25], or computing cumulative absorption over a region [26], what is required is an accurate absorption cross-section at a single, well-defined frequency. Given this, here we propose a quantum simulation algorithm that focuses on only getting this specific frequency dependent response, reducing the use of quantum resources relative to reconstructing the entire spectrum with full fidelity.

The most direct approach would involve constructing the resolvent  $(H - E_I - \omega + i\gamma)^{-1}$  and then evaluating the matrix element in Eq. (3). However, constructing matrix inverses is typically an expensive task on a quantum computer. Instead, we leverage the time-domain formulation of the same

matrix element that allows us to cast the same observable directly in terms of a (coherent) quantum simulation.

First, we re-write Eq. (3) using the discrete-time Fourier transform

$$\mathcal{G}_\mu(\omega) = \frac{\tau}{2\pi} \sum_{j=-\infty}^{\infty} e^{i\omega\tau j} \underbrace{e^{-\gamma\tau|j|} \langle \Psi_I | D_\mu e^{-iH\tau j} D_\mu | \Psi_I \rangle}_{\mathcal{G}_\mu(\tau j)}, \quad (7)$$

following Refs. [7, 24, 27]. Once cast in this form, we can further re-write it in a suggestive form

$$\mathcal{G}_\mu(\omega) = \langle \Psi_I | D_\mu \underbrace{\left[ \sum_{j=-j_{\max}}^{j_{\max}} p_{\omega,\gamma,\tau}(j) \left( e^{-i\hat{H}\tau} \right)^j \right]}_{\equiv G_t} D_\mu | \Psi_I \rangle, \quad (8)$$

where we define  $p_{\omega,\gamma,\tau}(j) = (\tau/2\pi)e^{-\gamma\tau|j|+i\omega\tau j}$  and introduced a cutoff  $j_{\max}$ . In this form, it is clear that for a finite range of  $j$ , the operator in the middle amounts to a polynomial of the one-step time evolution operator, and is in fact naturally a linear combination of unitaries (LCU). Implementing this operator and then performing, for example, a Hadamard test for the specific value of  $\omega = \omega_{\text{EUV}}$  would give direct access to the cross-section of interest in evaluating EUV sensitivity.

There are different strategies one could employ for preparing this polynomial operator: one approach could be to do so directly using the standard PREPARE-SELECT-PREPARE construction of an LCU (More details in Appendix A1). However, here we instead opt to use generalized quantum signal processing (GQSP) [28], where the individual time evolution unitaries will be implemented using a product formula. The high-level approach of the algorithm is as follows

1. Classically compute an approximate  $D_\mu |\Psi_I\rangle$  state and normalization factor  $\mathcal{N} = \|D_\mu |\Psi_I\rangle\|$ .
2. Initialize  $\frac{D_\mu}{\mathcal{N}} |\Psi_I\rangle$  state on the quantum computer using the sum-of-Slaters (SOS) method [29].
3. Use the GQSP algorithm to compute  $G_t$  applied to the initial state with a polynomial approximation of  $p_{\omega,\gamma,\tau}(j)$  for a given timestep propagator  $e^{-iH\tau}$  and  $j_{\max}$  cutoff. The propagator is implemented using a Trotter product formula.
4. Measure  $\mathcal{G}_\mu(\omega)$  in Eq. (8) using the Hadamard test for a given  $\epsilon$  error in the absorption cross section.

In the first step of the algorithm, we may choose from any standard technique for preparing an approximate ground state on a classical computer, such as the density matrix renormalization group (DMRG) method [30, 31] or selected configuration interaction [32, 33]. We assume the use of a Gaussian type orbital (GTO) basis set, but the algorithm will work for any choice of basis.

For the second step of the algorithm, we take the classical ground state wavefunction, and apply the dipole operator onto it, which can be efficiently performed by virtue of the fact the dipole operator is a one-body operator. We then take this dipole-acted state and prepare it on a quantum computer using the sum-of-Slaters (SOS) method [29]. The SOS state preparation approach for second quantized Hamiltonians in a GTO basis is typically orders of magnitude smaller in non-Clifford gate cost than the time evolution operator in the following step [24].

In the third step, we construct and implement the time evolution operator, which is the main source of the number of non-Clifford gates in the full algorithm. A key part of this step is the implementation of the individual time evolution unitaries  $e^{-iH\tau}$  for a single time step  $\tau$ . Rather than pursuing a qubitization-based strategy which would necessarily incur a dependency on the full one-norm of this Hamiltonian, we instead leverage compressed double factorization (CDF) [34–36] and a second order Trotter product formula to implement the unitary, following the approach of Ref. [24]. This entails factorizing the two-electron integrals as a sum of  $L$  individual Hamiltonian fragments, each of which takes a diagonal form  $Z^{(\ell)}$  in the basis defined by single-particle basis rotations  $U^{(\ell)}$

$$(pq|rs) \approx \sum_{\ell=1}^L \sum_{k,l=1}^N U_{pk}^{(\ell)} U_{ql}^{(\ell)} Z_{kl}^{(\ell)} U_{rl}^{(\ell)} U_{sl}^{(\ell)}. \quad (9)$$

The one-electron term can similarly be factorized as

$$(p|\kappa|q) = \sum_k \tilde{U}_{pk}^{(0)} \tilde{Z}_{kk}^{(0)} \tilde{U}_{qk}^{(0)}. \quad (10)$$

With the CDF approach, once the Jordan-Wigner mapping is employed, the Hamiltonian can be transformed into a sum of single-qubit and two-qubit Pauli  $Z$  rotations, interspersed with unitaries  $U^{(\ell)}$  that rotate many-body wavefunctions in the full Hilbert space in response to changing the single-particle basis by a  $U^{(\ell)}$  rotation. These unitaries

may be synthesized using Thouless' theorem [37, 38],

$$U^{(\ell)} = \exp \left( \sum_{p,q} [\log U^{(\ell)}]_{pq} (a_p^\dagger a_q - a_q^\dagger a_p) \right), \quad (11)$$

and subsequently implemented by decomposing it into Givens rotations [39].

The different fragments are diagonal in separate bases and as such do not commute with each other, nor with the fragment from the 1-electron Hamiltonian term. Given this, we implement the overall time evolution unitary by treating the different fragments with the second-order Trotter product formula. This incurs a Trotter error, which we estimate in the spectroscopic sense by controlling the maximum allowable deviation  $\Delta$  of the eigenvalues of the effective Hamiltonian being implemented by the product formula – namely, the original Hamiltonian plus a perturbative correction which is the commutator-based error from the approximate decomposition of the exponentials – from the true Hamiltonian's eigenvalues. For the second order formula, the leading error term is  $Y_3$ , given by Ref. [24]

$$Y_3 := - \sum_j \left[ \frac{[H_j, [\sum_{h<j} H_h, H_j]]}{24} + \frac{[\sum_{h<j} H_h, [\sum_{h<j} H_h, H_j]]}{12} \right] \quad (12)$$

while the effective Hamiltonian is

$$H' = H + \Delta^2 \sum_j \left[ \frac{[H_j, [\sum_{h<j} H_h, H_j]]}{24} + \frac{[\sum_{h<j} H_h, [\sum_{h<j} H_h, H_j]]}{12} \right] + \dots \quad (13)$$

Applying the perturbative approach to Trotter error estimation [24, 40] lets us deduce the expression

$$E'_l = E_l - \Delta^2 \langle E_l | Y_3 | E_l \rangle + O(\Delta^4), \quad (14)$$

for eigenvalue deviation in terms of the expected magnitude of the leading Trotter error  $|\langle Y_3 \rangle|$ . If we choose our desired error to be  $E'_l - E_l = \gamma$ , which is an input to the calculation determined by the requirements of our application, we can invert this expression to determine the maximum allowable Trotter step  $\Delta$ , namely  $\Delta = \sqrt{\gamma/|\langle Y_3 \rangle|}$ . Combined with the description of the CDF approach, the cost of implementing the time evolution for a given time step  $\tau$  can be computed in the same way as in Ref. [24], with the total cost being

$$\mathcal{C}_{\text{Trot}} = N_{\text{Trot calls}} \times L \times \mathcal{C}_{\text{fragment}}. \quad (15)$$

for  $N_{\text{Trot calls}} = 2$  calls to first-order Trotter step for a second order product formula,  $L$  CDF fragments, and the cost of a single fragment being given by the need to implement the  $2N(N-1)/2$  Givens rotations inherent in each basis transformation, and the  $2N(2N+1)/2$   $Z \otimes Z$  rotations inherent in the diagonal part of the fragment. The single-qubit rotations will be done using the phase gradient trick. The cost may be written as

$$\mathcal{C}_{\text{fragment}} = \mathcal{C}_{\text{unitary}} + \mathcal{C}_{Z\text{-matr}}, \quad (16)$$

with

$$\mathcal{C}_{\text{unitary}} = 2 \frac{N(N-1)}{2} (2\mathcal{C}_{\text{rot}}) + 2N\mathcal{C}_{\text{rot}}, \quad (17)$$

$$\mathcal{C}_{Z\text{-matr}} = \frac{2N(2N-1)}{2} \mathcal{C}_{\text{rot}} \quad \text{or} \quad 2N\mathcal{C}_{\text{rot}}. \quad (18)$$

Once the framework for implementing the timestep propagator  $U(\tau) = e^{-iH\tau}$  is constructed in the way described above, we need to implement  $G_t = \sum_j p_{\omega,\gamma,\tau}(j) (e^{-iH\tau})^j$  and we opt to use GQSP as a natural subroutine for this task. While standard quantum signal processing imposes parity constraints on the achievable polynomials, GQSP enables the direct embedding of an *arbitrary* complex polynomial  $P(U)$  of a unitary operator, which is necessary for representing  $p_{\omega,\gamma,\tau}(j)$ .

The algorithm employs  $U(\tau)$  as the signal operator within the GQSP ansatz. We classically compute  $d$  phase angles denoted  $\vec{\phi}$  required to synthesize the polynomial  $P(z) = \sum_{j=1}^d c_j z^j \approx \sum_{j=-j_{\text{max}}}^{j_{\text{max}}} (\tau/2\pi) e^{-\gamma\tau|j| + i\omega\tau j}$  approximating the Green's function. The resulting quantum circuit interleaves controlled- $U(\tau)$  operations on the system register with single-qubit rotations  $R(\phi_k)$  on an ancilla. The polynomial degree is  $d = j_{\text{max}}$ , determined strictly by the spectral resolution  $\gamma$  required to resolve the feature bandwidth.

The efficiency of the algorithm is governed by the subnormalization factor  $\beta$  in applying  $P(z)$  to the linear combination of timestep propagators  $U(\tau)$ , defined as the 1-norm of the polynomial coefficients. For the finite Fourier series truncation  $j_{\text{max}}$ , this sum can be derived analytically, starting with the triangle inequality

$$\beta = \sum_{j=-j_{\text{max}}}^{j_{\text{max}}} |p_{\omega,\gamma,\tau}(j)| \leq \frac{\tau}{2\pi} \sum_{j=-j_{\text{max}}}^{j_{\text{max}}} e^{-\gamma\tau|j|}. \quad (19)$$

Recognizing this as a geometric series symmetric about  $j = 0$ , we define  $r = e^{-\gamma\tau}$  and rewrite the sum as  $1 + 2 \sum_{j=1}^{j_{\text{max}}} r^j$ . Using the closed form for a geometric progression, we derive the upper bound

for  $j_{max}$  truncated  $\beta$  as

$$\beta \leq \frac{\tau}{2\pi} \left( \frac{1+r-2r^{j_{max}+1}}{1-r} \right) \quad (20)$$

In the limit of a large truncation cutoff ( $j_{max} \rightarrow \infty$ ), the term  $r^{j_{max}+1}$  vanishes. Applying the identity  $(1+e^{-x})/(1-e^{-x}) = \coth(x/2)$ , we recover the standard bound for arbitrary  $\beta$  as

$$\beta \leq \frac{\tau}{2\pi} \coth\left(\frac{\gamma\tau}{2}\right). \quad (21)$$

For the small time steps  $\tau$  ( $\gamma\tau \ll 1$ ), we can approximate  $\coth(x) \approx 1/x$ , yielding the scaling law  $\beta \approx 1/(\pi\gamma)$  used in our resource estimates.

Once the GQSP step is completed, the final step is to encompass the subroutines preparing the final state  $G_t D_\mu |\Psi_I\rangle$  in a Hadamard test. To explicitly quantify the measurement overhead for this entire algorithm, we reconstruct the absolute absorption cross-section  $\sigma_A(\omega)$  in the following way.

First, we classically compute the scalar electric dipole normalization factor  $\mathcal{N} = \|D_\mu |\Psi_I\rangle\|$ . In a given molecular orbital basis, evaluating this expectation value on the classical reference state scales polynomially with the number of orbitals, rendering the cost negligible. Second, we perform the aforementioned Hadamard test on the normalized dipole-excited state  $|\Phi\rangle = D_\mu |\Psi_I\rangle/\mathcal{N}$  utilizing the GQSP unitary  $U_{GQSP}$  to implement  $G_t$ . Then, we simply initialize the ancilla in the state  $\frac{1}{\sqrt{2}}(|0\rangle - i|1\rangle)$  and measure in the Pauli- $X$  basis to isolate the imaginary component, yielding a random variable  $Z \in \{-1, 1\}$ . Finally, the estimated physical absorption cross-section is reconstructed as

$$\bar{\sigma}_A(\omega) = \alpha \cdot \mathcal{N} \cdot \beta \cdot \mathbb{E}[Z], \quad (22)$$

where  $\alpha = \frac{4\pi\omega}{3c}$  is the semi-classical prefactor derived from the original absorption cross-section formula in Eq. (2).

The total cost is determined by the number of measurement shots ( $M$ ) required to resolve the target  $\sigma_A(\omega)$  to  $\epsilon$  accuracy with  $\bar{\sigma}_A(\omega)$ . The specific constant factors are governed by three application-specific parameters at the 92 eV operating frequency ( $\omega \approx 3.38$  a.u.). Using  $c \approx 137$  a.u., the prefactor is

$$\alpha \approx 0.10. \quad (23)$$

This term effectively suppresses the shot noise when converting to physical units for this specific target photon frequency. Additionally, we fix the spectral broadening to match the experimental bandwidth of

EUV sources at 2% of 92 eV as  $\gamma = 1.84$  eV (0.0676 a.u.) [41], which yields a subnormalization factor of

$$\beta \approx 1/(\pi\gamma) \approx 4.7. \quad (24)$$

Then, we can estimate the number of shots needed by choosing an error  $\epsilon$  in the final absorption cross section value in atomic units. Then the number of shots using the standard Chebyshev bound is

$$M = (\alpha\mathcal{N}\beta/\epsilon)^2 \quad (25)$$

## IV. PHOTOEMISSION SPECTRUM

### A. Background

Upon absorbing an EUV photon, a photoresist monomer can undergo an immediate photoionization event, instead of just a localized absorption, leaving the system in a highly excited non-stationary cationic state characterized by a core-level vacancy. This unstable configuration relaxes primarily through the Auger effect, a correlated two-electron process where a valence electron fills the core hole while transferring energy to a secondary electron, which is subsequently ejected into the ionization continuum.

The primary objective of the simulation presented in this section is to recover the kinetic energy distribution of these ejected electrons, denoted as the *photoemission spectrum*. As mentioned in the introduction, this distribution serves as the essential initial condition for multi-scale photolithography models, parameterizing the initial energies in stochastic electron cascades that eventually determine the blur width of the photoresist.

While the decay rate for a specific transition is formally described by Fermi's golden rule, relying on a perturbative framework to reconstruct the full spectrum is computationally intractable for complex molecules. Fermi's golden rule requires an explicit summation over the exponentially large manifold of final continuum eigenstates to resolve the energy distribution. Furthermore, standard quantum chemistry methods rely on localized Gaussian basis sets, which cannot accurately represent these high-energy, delocalized scattering states.

Therefore, we adopt a non-perturbative, real-time quantum simulation approach to directly simulate the Auger decay process. Instead of summing over individual eigenstates, we simulate the time evolution of the correlated many-body wavefunction in a plane-wave basis using a first quantized representation of the electrons. This naturally generates the

superposition of all accessible final states within a chosen simulation cell with a large enough volume to represent the vacuum. We then extract the photoemission spectrum directly by projecting the evolved state onto the continuum subspace and then measuring the kinetic energy in the planewave basis. In general, this procedure contains the kinetic energy of both photoionized electrons at short times (subfs), and then Auger electrons later in time, but the ionization spectra could be subtracted out from the final time  $t$  spectrum to isolate the Auger spectrum specifically. Since this is not a bottleneck, we do not discuss it further in this work for simplicity. Before detailing the full simulation algorithm, we start with a quick overview of first quantized quantum simulations in the next subsection.

### B. First quantization

In a first-quantized plane wave representation for electronic structure, the quantum state is encoded in  $\eta$  registers corresponding to each electron's momentum, with the total state vector antisymmetrized to satisfy fermionic statistics. For simplicity, using similar notation to Ref. [42], the system can be defined within a cubic cell of volume  $\Omega$ , utilizing a basis of  $N$  plane waves per electron with reciprocal lattice vectors

$$k_p = \frac{2\pi p}{\Omega^{1/3}} \quad \text{where} \quad (26)$$

$$p \in G = \left[ -\frac{N^{1/3}-1}{2}, \frac{N^{1/3}-1}{2} \right]^3 \cap \mathbb{Z}^3.$$

The kinetic energy operator,  $T$ , is diagonal in the plane wave basis:

$$T = - \sum_{i=1}^{\eta} \sum_{p \in G} \frac{\|k_p\|^2}{2} |p\rangle\langle p|_i \quad (27)$$

where  $|p\rangle\langle p|_i$  acts on the register of the  $i$ -th electron, acting as the identity elsewhere. The electron-nuclear attractive potential,  $U$ , is

$$U = -\frac{4\pi}{\Omega} \sum_{i=1}^{\eta} \sum_{l=1}^L \sum_{p,q \in G, p \neq q} \zeta_l \frac{e^{ik_{q-p} \cdot \mathbf{R}_l}}{\|k_{p-q}\|^2} |p\rangle\langle q|_i \quad (28)$$

and the electron-electron repulsion,  $V$ , couples momentum states via transfer vectors  $\nu$ :

$$V = \sum_{1 \leq i < j \leq \eta} \frac{4\pi}{\Omega} \sum_{\substack{p,q \in G \\ \nu \in G_0}} \frac{1}{\|k_\nu\|^2} |p+\nu\rangle\langle p|_i |q-\nu\rangle\langle q|_j. \quad (29)$$

The momentum transfer vectors are drawn from the set  $G_0 = G \setminus \{(0,0,0)\}$ . This representation and Hamiltonian definition will be assumed throughout Section IV, unless otherwise noted.

### C. Algorithm

To target the kinetic energy spectra of photoemitted electrons, one must devise a type of decision boundary in real space for determining if an electron is in the continuum or not. Then, one can compute the kinetic energy spectrum of these ejected electrons after applying this projection. We construct a correlation function for this task of the following form

$$C(t, \tau) = \langle \Psi_0 | W e^{iHt} \Pi_c e^{-iT\tau} \Pi_c e^{-iHt} W | \Psi_0 \rangle, \quad (30)$$

where  $|\Psi_0\rangle$  is the electronic ground state,  $W$  is the light matter state preparation operator, including the windowed electric dipole,  $t$  is the real simulation time,  $\Pi_c$  is a continuum projection operator,  $\tau$  is the spectral time length to resolve the signal, and  $T$  is the electronic kinetic energy operator. One benefit of the planewave basis representation of the system is that the correlation function in Eq. (30) can be simplified to

$$C(t) = \langle \Psi_0 | W e^{iHt} \Pi_c |k\rangle\langle k| \Pi_c e^{-iHt} W | \Psi_0 \rangle = |\langle k | \Pi_c e^{-iHt} W | \Psi_0 \rangle|^2 \quad (31)$$

since we can measure the electron's kinetic energy directly in the kinetic energy basis, represented by  $|k\rangle$ .

In summary, this correlation function takes the initial electronic ground state for the system, uses  $W$  to excite system with semi-classical light matter interaction at 92 eV, simulates the electron dynamics to time  $t$ , and then measures the kinetic energy of electronic degrees of freedom in the continuum. For this correlation function we choose  $t$  to cover the typical femtosecond lifetime of Auger decay, with more details of the numerics explained in Section V.

The algorithmic steps detailed below, mimic the terms in the correlation function Eq. (31). Broadly speaking, Eq. (31) describes a kind of pump-probe spectroscopy. First, the material is excited with the incident radiation. Then, for a delay time  $t$ , the material undergoes its natural Hamiltonian dynamics. Finally, a probe of incident radiation is then used to measure the kinetic energy of any electrons that are ejected from the material system (modeled by our direct kinetic energy basis measurement). Our algorithm proceeds by emulating each of these steps.

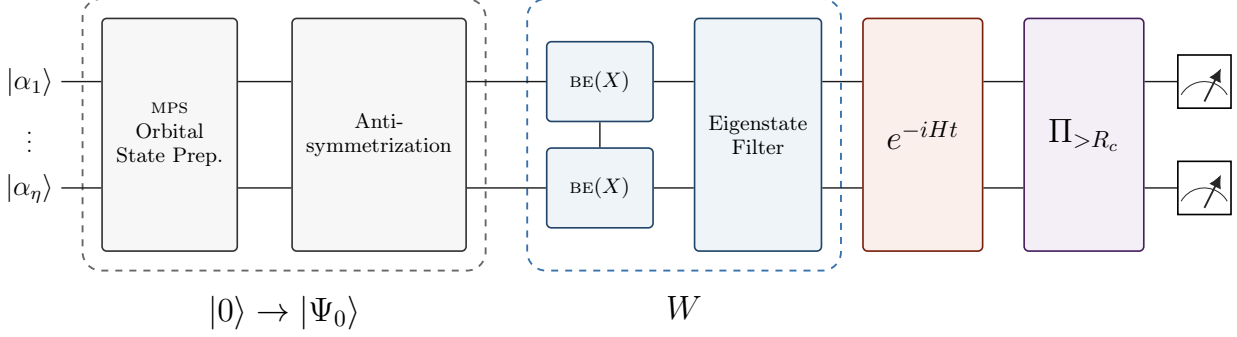


FIG. 2. Quantum circuit schematic for simulating the photoemission spectrum in a first-quantized plane-wave basis. The simulation operates on  $\eta$  particle registers initialized as  $|\alpha_1\rangle \cdots |\alpha_\eta\rangle$ , where each  $\alpha$  represents the integer index encoding the momentum coordinates of a single electron. The algorithm proceeds in four main stages: (1) State Preparation: The electronic ground state  $|\Psi_0\rangle$  is synthesized from a compressed MPS representation of molecular orbitals, with antisymmetrization applied to enforce fermionic statistics. (2) Excitation ( $W$ ): The electric dipole operator creates the superposition of excited states, using block-encoded position operators ( $\text{BE}(X)$ ) and Quantum Signal Processing to filter for eigenstates within the 92 eV bandwidth. (3) Time Evolution ( $e^{-iHt}$ ): The wavefunction is propagated for time  $t$  to simulate the Auger decay dynamics. (4) Measurement: A real-space projector  $\Pi_{>R_c}$  identifies electrons in the continuum. Because the kinetic energy operator is diagonal in the plane-wave basis, the final kinetic energy spectrum is extracted by directly sampling the computational basis of these particle registers. Note that for visual clarity, the extensive ancilla registers required for block encodings and arithmetic subroutines are omitted from this high-level schematic.

Starting from the ground state of the material system, we apply the dipole operator  $D_\mu$ , which accurately models the material response to broadband radiation in the non-relativistic regime. The action of  $D_\mu$  on  $|\Psi_0\rangle$  induces a linear combination of excited states weighted by their transition probabilities as given by Fermi’s golden rule. Since we have a complete basis spanning bound and continuum states, applying the dipole operator generates states of both types of character. To emulate the response from a coherent light source with a particular incident frequency, we perform a variant of eigenstate filtering to apply a Gaussian filter function to the spectrum of the material Hamiltonian centered around the 92 eV central frequency of the radiation. The square root of the Gaussian standard deviation parameter  $\sigma$  being proportional to the full width at half of maximum (FWHM) of the Gaussian pulse, i.e.,  $\sigma = 2\sqrt{2\ln(2)}\text{FWHM}$ . This constructs the  $W$  operator of Eq. (31).

Following this, we perform the Hamiltonian dynamics that may induce Auger decay. After time  $t$ , we then measure the kinetic energy spectrum of the electrons that are delocalized from the material as a result of the Auger decay process. This is obtained by applying a projection operator in real space corresponding to a predetermined cutoff radius distinguishing between those degrees of freedom that are labeled as “bound” to and “unbound” from the molecular system. The success probability of being in the

“unbound” subspace gives the probability of observing an electron in the continuum, and sampling the wavefunction in this same subspace provides the kinetic energy spectrum of the continuum wavefunction as a histogram. We summarize these steps in the numbered list below each corresponding to a following subsection:

1. Prepare the first quantized ground state from an approximate classical reference in second quantization using the method of Ref. [43].
2. Apply the dipole operator  $D_\mu$  to excite the ground state into a linear combination of excited states.
3. Filter excited states to those that differ from the ground state energy by  $\sim 92\text{eV}$ .
4. Perform time evolution of system for  $\sim 1-10\text{fs}$  to allow for Auger decay.
5. Using a real space boundary, measure kinetic energy of the continuum electronic degrees of freedom.

For a more detailed graphical depiction of the algorithm at a high level, see Fig. 2.

### 1. State Preparation

The first step of our algorithm concerns the preparation of the electronic ground state of the target system upon which the dipole operator will be applied. We assume that for typical molecular systems, and clusters more generally, we start by computing the Hartree-Fock molecular orbitals using a Gaussian basis set, standard in classical quantum chemistry simulation codes. Then, based on this molecular orbital basis, we can choose a single, or multi-Slater determinant representation of the ground state in second quantization, generally described as

$$|\Psi_0^{SQ}\rangle = \sum_s^S c_s |s\rangle \quad (32)$$

where  $s$  is the Slater determinant index in second quantization,  $S$  is the total number of Slater determinants and  $c_s$  is the normalized (real) coefficient. Assuming we have this object precomputed from a chosen classical method, the bottleneck of the state preparation routine is to then transform the compact second quantized ground state,  $|\Psi_0^{SQ}\rangle$ , in the Gaussian orbital basis, to the first quantized representation in the plane wave basis,  $|\Psi_0\rangle$ .

We employ one state-of-the-art approach introduced in Ref. [43] to prepare molecular ground states in a first-quantized plane wave basis from a second quantized ground state in a Gaussian basis. This approach circumvents the prohibitive scaling of naive first quantized plane wave state preparation, which scales as  $O(\eta N)$ , by mapping molecular orbitals derived from classical Gaussian basis calculations into a compact Matrix Product State (MPS) form.

The core of the algorithm is the synthesis of a single-particle basis transform unitary,  $V$ , which maps the computational basis states of the first quantized electron registers to the target MPS-compressed orbitals as a linear combination of plane wave basis states using standard unitary synthesis techniques. For an  $\eta$ -electron system, the total non-Clifford gate complexity is dominated by the implementation of this transformation across all registers ( $V^{\otimes \eta}$ ), scaling as

$$C_{sp} \in \tilde{O}(\eta K_{mo} g^{3/2} \text{polylog}(N)), \quad (33)$$

where  $K_{mo}$  is the number of molecular orbitals,  $g$  is the size of the Gaussian basis counting all primitives contained within each orbital basis function, and  $N$  is the size of the plane wave basis. In almost all cases  $K_{mo}, g \ll N$ . Notably, the cost scales only polylogarithmically with the plane wave basis size,  $N$ ,

enabling high-precision discretizations for the state preparation step at relatively minimal cost.

Crucially, the overhead for preparing correlated states beyond a single Slater determinant (e.g., from configuration interaction, DMRG, etc.) is subdominant to preparing the basis transformation operator. This efficiency arises because the computationally expensive basis transformation acts as a fixed dictionary that maps orbital indices to physical wavefunctions; its circuit complexity is determined solely by the number of orbitals in the basis, not by the specific superposition of indices present in the input state. Consequently, once the low-cost initial superposition of integer indices is prepared [44], the dominant cost of synthesizing the physical orbitals remains similar to that of the Hartree-Fock state. Constant factors and polynomial overheads associated with the MPS compression are rigorously minimized and verified using the `orb2mps-fq` software library of Ref. [43], which demonstrates resource reductions of orders of magnitude for this state preparation task.

### 2. Application of electric dipole operator

The electric dipole operator is obtained by the dot product of the external electric field, representing the classical light, with the position operator of the system. Let us denote the time dependent external electric field as

$$\mathbf{E}(t) = \begin{pmatrix} E_x(t) \\ E_y(t) \\ E_z(t) \end{pmatrix} \quad (34)$$

where  $t \geq 0$  and each  $E_j(t) \in \mathbb{C}$ . Under the dipole approximation, the light-matter interaction is given by the time-independent Hamiltonian

$$H_I = \sum_{j \in \{x,y,z\}} \sum_{i \in [\eta]} |E_j| e^{i\phi_j} \hat{x}_j^{(i)}, \quad (35)$$

where  $\hat{x}_j^{(i)}$  is the *position* operator in real space, which acts on spatial direction  $j \in \{x, y, z\}$  of particle  $i$ . Since the electric field is just a constant number ( $c$ -number) scaling the quantum mechanical operator  $\hat{x}_j^i$ , its implementation is straightforward. We will focus on the cost to construct a block encoding of a discretization of position operator on a real-space grid. Let  $\Omega^{1/3} > 0$  characterize a side length of the ‘‘simulation box’’, and discretize the volume  $\Omega = [-\Omega^{1/3}/2, \Omega^{1/3}/2]^3$  into  $N$  equispaced unit voxels of the form  $\mathbf{x} = \frac{\Omega^{1/3}}{N^{1/3}}(i, j, k)$

where  $i, j, k \in [N^{1/3}]$ . For simplicity, we will always take  $N^{1/3} \equiv 2^n$ , so that on the quantum computer, the position register of each electron is encoded into exactly  $3n$  qubits. We will denote a single electron register as  $|\alpha^i\rangle := |\alpha_x^i\rangle |\alpha_y^i\rangle |\alpha_z^i\rangle$ , where each  $\alpha_j^i \in \{0, 1\}^n$  encoding an integer in  $[N^{1/3}]$ . For  $\eta$  electrons, we will write a basis state in the combined system register of  $3\eta n$  qubits as  $|\alpha\rangle := |\alpha^0\rangle |\alpha^1\rangle \dots |\alpha^{\eta-1}\rangle$ .

We define the *discrete position operator*, a finite dimensional matrix that is diagonal in the position basis, as

$$X_j^i |\alpha\rangle = \frac{\text{int}(\alpha_j^i) \Omega^{1/3}}{N^{1/3}} |\alpha\rangle, \quad (36)$$

where  $\text{int} : \{0, 1\}^n \rightarrow [2^n]$ . Since  $X_j^i$  only acts non-trivially on the  $j$ th dimension register of particle  $i$ ,  $X_j^i$  takes the form of a one-body operator

$$X = \frac{\Omega^{1/3}}{N^{1/3}} \text{diag}\left(0, 1, \dots, N^{1/3} - 1\right), \quad (37)$$

embedded into the many-body Hilbert space by tensoring with the identity on all other degrees of freedom.

For both this step, and the time evolution of the system, we will access the position operator and electronic structure Hamiltonian as *block encodings*. A block encoding works by embedding a non-unitary matrix  $A$ , scaled by a quantity  $\lambda$  we call the subnormalization factor ensuring  $\|A/\lambda\| \leq 1$ , into the top-left block of a non-unitary matrix  $U_A$ . Using  $m \geq 1$  ancilla qubits, we say that  $U_A$  is an  $(\lambda, m, \epsilon)$ -BE( $A$ ) if  $\|A - I \otimes \langle 0_m | U_A I \otimes | 0_m \rangle\| \leq \epsilon$ . Block encoding, and the related quantum signal processing (QSP) [45, 46], allow us to efficiently implement functions of block encoded matrices and in turn is a widely applicable protocol for quantum algorithms. The main primitives to realize the block encodings in this work are the SELECT and PREPARE routines. Since these routines are common in the quantum algorithms literature, we reserve the definitions of SELECT, PREPARE, and the block encoding concept more generally, to the Appendix A 1.

To implement a block encoding of

$$X^{(\eta)} := \sum_{j=1}^3 \sum_{i=0}^{\eta-1} X_j^i, \quad (38)$$

we perform the following operations

1. Prepare a uniform superposition over  $3\eta$  many degrees of freedom, with non-Clifford cost  $\lceil \log(3\eta) \rceil + 2 \log(1/\epsilon)$ .

2. Control swaps of a single degree of freedom into an  $n$  qubit ancilla register. This requires  $3\eta n$  Toffoli gates.
3. Perform an  $n$  qubit quantum Fourier transform on ancilla register using addition into a phase gradient state. This requires  $n(n-1)$  Toffoli gates.
4. Apply  $X$  using inequality testing. This requires  $n$  Toffoli gates.
5. Uncompute steps (1-3)

The inequality testing technique used in Step 3, introduced in Ref. [47], is described in Appendix A 2. Since steps (1-3) can be uncomputed without Toffoli cost using the “measure-and-fixup” construction from Ref. [48], the overall non-Clifford cost to apply the above operations to implement an  $(\eta N^{1/3}, 1, \epsilon)$ -BE( $X^{(\eta)}$ ) is

$$\mathcal{C}_X = n(n + 3\eta - 1) + \lceil \log(3\eta) \rceil + 2 \log(1/\epsilon). \quad (39)$$

We remark that the measure-and-fixup construction requires as many ancilla qubits as there are Toffoli gates. However, since the number of ancilla qubits used to block encode the electronic structure Hamiltonian far outnumbers the Toffoli gates (and thereby the number of ancilla) needed to implement the measurement based uncomputation of these protocols, we may always assume that the uncomputation can be performed without additional non-Clifford cost.

### 3. Windowed Dipole operator

To emulate the material response from the interaction with the incident EUV radiation occurring at a specific frequency, we will apply an eigenstate filter to study electronic dynamics restricted to a subspace of energies that could interact with radiation of a particular frequency. The energy of the incident light is 92 eV ( $\approx 3.38$  Ha), and therefore cannot induce transitions between eigenstates of the matter Hamiltonian with energy differences significantly far from 92 eV. Typical EUV experiments show that the FWHM of the incident radiation bandwidth is 2% of the 92 eV energy [41], which, for a coherent light source, corresponds to a Gaussian with a standard deviation of 1.84 eV. In turn, this corresponds to a desired energy resolution of  $\delta \equiv 0.067$  Ha and  $\delta^{-1} \sim 15$  Ha $^{-1}$ .

In order to compute the energy differences required for measuring transition energies, we straightforwardly modify the block encoding of the electronic Hamiltonian by an additive shift of  $-\lambda_0 I$ ,

where  $\lambda_0$  is the ground state energy estimate of the initial state, in which we can use the computed estimate from the second quantized approach of the classical algorithm piece of the routine in step 1. With this ground state energy value in hand, this shift can be accounted for in the block encoding of  $H$  with negligible additional complexity to that of block encoding  $H$ . This is more efficient than block encoding  $H$  and performing a linear combination of block encodings to implement a block encoding of  $H - \lambda_0 I$ .

To implement the filtering, we begin with this ground-state shifted block encoding of the electronic structure Hamiltonian. We will denote the non-Clifford cost to implement the SELECT and PREPARE portion of the block encoding as  $C_{\text{SEL}}$  and  $C_{\text{PREP}}$  respectively, these costs are reported in Eqs. (41) and (42). This block encoding is very involved, and the majority of the operations have been described and optimized in great detail in Ref. [42]. We follow the notation of this work, and parameters such

as  $n_M, n_\eta$ , etc. that are introduced below are described in Table IV of Appendix B of this work as well as in Appendix A of the original reference [42]. Now, to emulate the response due to the interaction with a coherent light source, we employ a Gaussian filter function on the block encoding. We target a Gaussian centered around  $\mu = \frac{3.38}{\lambda}$  Ha with standard deviation  $\sigma \frac{\delta}{\lambda}$ . The complexity to perform this task is dictated by the convergence rate of the polynomial approximation to this Gaussian, which is  $\approx \frac{\lambda}{2\sqrt{2\ln(2)\delta}} \log\left(\frac{1}{\epsilon}\right)$ , where  $\epsilon$  here controls the error at the level of the polynomial approximation.

The overall non-Clifford cost to perform the quantum signal processing is

$$C_W = \frac{\lambda(C_{\text{SEL}} + C_{\text{PREP}} + c_{\text{ref}})}{\delta 2\sqrt{2\ln(2)}} \log\left(\frac{1}{\epsilon}\right), \quad (40)$$

where  $c_{\text{ref}} = n_{\eta\zeta} + 2n_\eta + 6n + n_M + 16$  is the total number of ancilla qubits that need to be reflected against in the block encoding. The gate complexity of the preparation routine and selection routine is

$$C_{\text{PREP}} = \underbrace{2n^2 + 15n + 4n_M(n+1) - 7 + \lambda_\zeta + \min_k([2^{-k}\lambda_\zeta] + 2^k)}_{\text{PREP}_{UV}} + \underbrace{2(n+9)}_{\text{PREP}_T} + \underbrace{2(n_T + 4n_{\eta\zeta} + 2b_r - 12) + 14\eta + 8b_r - 36}_{\text{PREP}_{TUV}} \quad (41)$$

$$C_{\text{SEL}} = \underbrace{24n + 6nn_R}_{\text{SEL}_{UV}} + \underbrace{5(n-1) + 2}_{\text{SEL}_T} + \underbrace{12\eta n - 4\eta - 8}_{\text{SEL}_{TUV}}, \quad (42)$$

where  $\text{PREP}_{UV}$  (resp.  $\text{SEL}_{UV}$ ) characterizes the cost to implement the prepare circuit for the potential terms,  $\text{PREP}_T$  the cost of the prepare circuit for the kinetic term, and  $\text{PREP}_{TUV}$  the cost of the prepare circuit that combines  $T$  and  $U + V$  into the prepare circuit for  $H$ . The parameters  $n_R, n_T, n_M$ , and  $b_r$  are described in Table IV of Appendix B.

A consequence of performing these non-unitary operations is that we incur a success probability overhead. At the level of applying the dipole operator, supposing we have some success probability  $P_d$ , we would need to apply the quantum circuit for the dipole operator and state preparation  $O(1/\sqrt{P_d})$  using amplitude amplification. Then, for the filtering, supposing we have some probability of  $P_w$  of successfully applying the filter function, we would need to repeat the quantum circuit that applied the filter and the quantum circuit that applied the dipole

$O(1/\sqrt{P_w})$  many times. Overall, including the success probability, the number of gates needed to perform this step is

$$C_{\text{filter}} = O\left(\frac{1}{\sqrt{P_w}} \left(C_W + \frac{1}{\sqrt{P_d}}(C_X + C_{\text{sp}})\right)\right).$$

#### 4. Time Evolution

This is by far the costliest portion of our algorithm, but is also the most well-developed subroutine we use in this work. We use a quantum signal processing (QSP) based approach to implement the time evolution operator [28, 45, 49], and the cost can be straightforwardly obtained by taking the block encoding costs of Eq. (41) and (42) and the polynomial degree required to approximate the function

$e^{i\lambda t}$ . By Corollary 62 of Ref. [46], the polynomial degree is bounded by

$$d \leq 2\lambda t + 3\log(12/\epsilon), \quad (43)$$

where  $\lambda$  is the block encoding subnormalization factor, and  $\epsilon$  controls the error in the implementation of  $e^{iHt}$  at the level of the polynomial approximation. This  $\epsilon$  does not control, for example, the error in the block encoding of  $H$  itself. Of course, the overall error in  $e^{iHt}$  can be obtained by ensuring that  $H$  is implemented as a block encoding with error  $\epsilon/2$  and  $e^{iHt}$  is approximated with error  $\epsilon/2$  and applying a triangle inequality.

Then, applying Eq. (43), and the block encoding costs in Eqs. (41) and (42), we obtain a non-Clifford gate cost of

$$\mathcal{C}_{t\epsilon} = (2\lambda t + 3\log(12/\epsilon)) (\mathcal{C}_{\text{SEL}} + 2\mathcal{C}_{\text{PREP}} + c_{\text{ref}}) \quad (44)$$

to perform the time evolution up to time  $t$ .

### 5. Measurement

Finally, our goal is to extract the distribution of kinetic energies of electrons that are emitted from the molecule into the continuum. We use a sphere centered at the origin in real space (i.e., at  $(0, 0, 0)$ ) with a fixed radius  $R_c$  to bifurcate the configuration space into “bound” and “continuum”. This provides a quantitative decision boundary; any electronic degree of freedom with real-space coordinate  $x$  satisfying  $\|x\| \geq R_c$ , belonging to the “continuum”, otherwise belonging to the localized molecular bound states. We choose a hard cutoff for simplicity, but soft boundary extensions would be straightforward, similar to classical simulation methods applied to small models of photoelectron emission in the literature [50]. The choice of  $R_c$  is dependent on the molecular system and the energy of the initial state. For now, we will assume that  $R_c$  is a given fixed constant.

Let us recall the lattice of points

$$q \in \left[ -\frac{N^{1/3}-1}{2}, \frac{N^{1/3}-1}{2} \right]^3 \equiv G \subset \mathbb{Z}^3, \quad (45)$$

where a point in the real space is given by

$$r_q = \frac{\Omega^{1/3}}{N^{1/3}} q. \quad (46)$$

Applying the inverse quantum Fourier transform to a point  $|p\rangle$  in the reciprocal space yields a superposition of points  $q$  in the real space. Each point  $q \in G$ ,

is associated with the tuple of integers  $(q_x, q_y, q_z)$ , with each  $q_j$  a binary value encoding the subset of integers  $\left[ -\frac{N^{1/3}-1}{2}, \frac{N^{1/3}-1}{2} \right] \cap \mathbb{Z}$ . The element is mapped to the associated position in the discretized real space by the scaling factor  $\frac{\Omega^{1/3}}{N^{1/3}}(q_x, q_y, q_z)$ . Using this relation, we can determine if  $q \in G$  lies inside a sphere of radius  $R_c > 0$  by checking the inequality,

$$q_x^2 + q_y^2 + q_z^2 < \left( \frac{R_c N^{1/3}}{\Omega^{1/3}} \right)^2. \quad (47)$$

Notice that in contrast to the position operator, we need to test if the norm of a vector in 3 spatial dimensions satisfies the inequality (47). This necessitates performing a quantum Fourier transform on  $3n$  qubits instead of just  $n$ , since we need to map from the 3-dimensional momentum space to the 3-dimensional position space. Thus, the quantum Fourier transform needed to implement this subroutine is more costly than that used in the position operator. The overall costs to perform each subroutine to realize this operation for a single electron are

1. Quantum Fourier transform to switch into the position basis. This requires  $3n(3n-3)$  Toffoli gates
2. Summation of three squares. This requires  $3n^2 - n - 1$  Toffoli gates
3. Test inequality in Eq. (47). This requires  $2n+2$  Toffoli gates
4. Uncompute (1-2).

We can once again uncompute steps 1 and 2 without Toffoli cost, using the same technique from earlier [48], leading to a total Toffoli cost of  $12n^2 - 8n + 1$ . We combine the above steps into a single subroutine we denote as BOUND?, which performs the operation

$$|q\rangle |0\rangle \xrightarrow{\text{BOUND?}} |q\rangle |b(\|q\| < R_c)\rangle, \quad (48)$$

where  $b(\text{false}) = 0$  and  $b(\text{true}) = 1$ . This notation neglects explicitly writing out the ancilla registers that are used and uncomputed along the way, as described above.

For the many body case, the decision boundary becomes if there is any single electron register in the continuum. To test for this, we can simply append an ancilla register of  $n_\eta = \lceil \log(\eta) \rceil$  qubits, then perform steps 1-3 above, and controlling on the  $|0\rangle$  state of the flag qubit  $|b(\|q_i\| < R_c)\rangle$  in Eq. (48), perform controlled addition of  $+1$  into the  $n_\eta$  qubit ancilla register and uncompute steps 1-3. Repeating this operation  $\eta$  many times, and with a flag qubit set

Photoemission Spectrum Algorithm Subroutines		
Symbol	Cost	Description
$\mathcal{C}_{sp}$	$\tilde{O}(\eta K_{mog}^{3/2} \text{polylog}(N))$	Initial state preparation (Constant factors computed via <code>orb2mps-fq</code> library of Ref. [43])
$\mathcal{C}_X$	$n(n + 3\eta - 1) + \lceil \log(3\eta) \rceil + 2 \log(1/\epsilon)$	Block encoding of position operator used to apply dipole operator
$\mathcal{C}_{\text{PREP}}$	Eq. (41)	Cost to implement PREPARE circuit in block encoding of $H$
$\mathcal{C}_{\text{SEL}}$	Eq. (42)	Cost to implement SELECT in block encoding of $H$
$\mathcal{C}_{\text{BOUND?}}$	$\eta(12n^2 - 8n + \lceil \log(\eta) \rceil + 1)$	Projector onto “continuum” real-space degrees of freedom
$\mathcal{C}_W$	$\frac{\sqrt{2}\pi\lambda(\mathcal{C}_{\text{SEL}} + 2\mathcal{C}_{\text{PREP}} + c_{\text{ref}})}{\delta} \log\left(\frac{1}{\epsilon}\right)$	Gaussian eigenstate filter from dipole excited ground state
$\mathcal{C}_{te}$	$(2\lambda t + 3 \log(\frac{12}{\epsilon})) (\mathcal{C}_{\text{SEL}} + 2\mathcal{C}_{\text{PREP}} + c_{\text{ref}})$	Time evolution of the system Hamiltonian with normalization factor $\lambda$ for some time $t$ .

TABLE I. The non-Clifford gate costs of the main subroutines used in the photoemission simulation algorithm.

to the  $|0\rangle$  state, we control on the all zero state of the  $n_\eta$  qubit register to apply an  $X$  gate to the flag. Depending on the qubit budget, it is also possible to remove the costs associated with performing controlled addition by 1 by using  $\eta$  ancilla qubits to flag each register as bound  $|0\rangle$  or continuum  $|1\rangle$ , and apply an  $\eta$  qubit controlled Toffoli on the all-ones state of the  $\eta$  flag qubits onto a single ancilla qubit. This results in a Toffoli cost of  $\eta$  as opposed to the  $\eta \log(\eta)$  cost in the former approach. In either case, we may combine the above steps into the operator ALL-BOUND?, which performs the operation

$$|q^{(n)}\rangle |0\rangle \xrightarrow{\text{ALL-BOUND?}} |q^{(n)}\rangle \left| \prod_{i=0}^{\eta-1} b(\|q_i\| < R_c) \right\rangle, \quad (49)$$

where we introduced the shorthand notation  $|q^{(n)}\rangle \equiv |q_0, q_1, \dots, q_{\eta-1}\rangle$ .

Applying this operation to a superposition performs a projection

$$\begin{aligned} |\psi\rangle &= \sum_{q^{(n)}} \psi(q^{(n)}) |q^{(n)}\rangle |0\rangle \\ \xrightarrow{\text{ALL-BOUND?}} & \sum_{q^{(n)}: \exists \|q_i\| \geq R_c} \psi(q^{(n)}) |q^{(n)}\rangle |0\rangle + \quad (50) \\ & \sum_{q^{(n)}: \nexists \|q_i\| \geq R_c} \psi(q^{(n)}) |q^{(n)}\rangle |1\rangle \\ &= \Pi_{\text{cont}} |\psi\rangle |0\rangle + \Pi_{\perp} |\psi\rangle |1\rangle, \end{aligned}$$

where  $\Pi_{\text{cont}}$  is the projector onto the subset of the many-body wavefunction where *any* particle has a position coordinate with radius larger than or equal to  $R_c$ , and  $\Pi_{\perp}$  the projector onto the set of states where *all* particle position coordinates have radius less than  $R_c$ . Overall, the operation ?ALL-BOUND is just  $\eta$  times the cost for a single particle plus a factor of  $\log(\eta)$  to perform the the controlled addition, and can therefore be realized with non-Clifford cost

$$\mathcal{C}_{\text{BOUND?}} = \eta(12n^2 - 8n + \lceil \log(\eta) \rceil + 1). \quad (51)$$

As before, application of a non-unitary operation will incur some success probability overhead. Were the algorithm to fail at this stage, we would need to reflect against all the other steps of the algorithm, leading to a cost of

$$\mathcal{C}_{\text{tot}} = \frac{1}{\sqrt{P_c}} (\mathcal{C}_{\text{BOUND?}} + \mathcal{C}_{te} + \mathcal{C}_{\text{filter}}),$$

which would be catastrophic if  $P_c$  were small. However, the success probability of this step is manageable. Firstly, the success state corresponds to the condition where *any* electronic degree of freedom is supported outside the spherical region, whereas the failure state only occurs when *all* electronic degrees of freedom are confined in the bound region. Thus, there are many more potential configurations in the success subspace than the failure subspace. Secondly, photoelectron ionization simulations emerge from the need to better understand an experimentally observed phenomenon for the system we are

simulating, implying that these processes occur with non-vanishing probability. Thus, we take as an assumption that the success probability of the continuum projector is a negligible prefactor in the cost of our algorithm.

Now by applying the operations that we discussed above we have created the state

$$\Pi_{\text{cont}} e^{-iHt} W |\Psi_0\rangle, \quad (52)$$

omitting normalization factors. Now, we can simply sample from this post-selected state to estimate the distribution of single-particle kinetic energies of the continuum electronic degrees of freedom. From each particle register  $i$  we measure and obtain a momentum vector  $k_i$ . We then classically compute the quantity  $\frac{\|k_i\|^2}{2}$ . From each measurement of the device, we recover  $\eta$  many samples from the single particle distribution. We can define the joint statistic

$$T^{(k)} = \frac{1}{\eta} \sum_{i=0}^{\eta-1} T_i^{(k)}, \quad (53)$$

where

$$T_i^{(k)} = \begin{cases} 1 & \text{register } i \text{ has kinetic energy } k \\ 0 & \text{else.} \end{cases}$$

Since each  $T_i^{(k)}$  is binary, the sampling-based estimator is a Bernoulli process with probability  $p = \mathbb{E}[T^{(k)}]$ , and variance  $\sigma^2 = p(1-p) \leq \frac{1}{4}$ .

For a fixed number of samples  $M$ , obtaining samples  $T_j^{(k)}$ , we have the estimator

$$\hat{p}(k) = \frac{1}{M} \sum_{j=1}^M T_j^{(k)}. \quad (54)$$

The variance is,

$$\text{Var}(\hat{p}(k)) = \frac{\text{Var}(T^{(k)})}{M} = \frac{\sigma^2(1 + (\eta - 1)\rho)}{\eta M},$$

where the last equality results from the fact that for a linear combination of statistics  $T' = \sum_{i=1}^{\eta} a_i T'_i$  we have

$$\text{Var}(T') = \left[ \sum_{i=1}^{\eta} a_i \text{Var}(T'_i) + \sum_{i \neq j} a_i a_j \text{Cov}(T'_i, T'_j) \right].$$

Then, with  $a_i = a_j = \frac{1}{\eta}$ , for identical particles  $\text{Cov}(T_i, T_j) = \rho\sigma^2$  for all  $i, j$  and  $\text{Var}(T_i) = \sigma^2$  for all  $i$ , we obtained the desired statement.

Now, to bound the sampling complexity, we can apply Bernstein's inequality

$$\mathbb{P} \left( \left| \frac{1}{M} \sum_{i=1}^M T_i^{(k)} - \mathbb{E}[T^{(k)}] \right| \geq \epsilon \right) \leq 2 \exp \left( -\frac{M\epsilon^2}{2v + \frac{2}{3}\epsilon} \right), \quad (55)$$

the samples  $T_i$ , with variance upper bounded by  $v$ . Thus to achieve error  $\epsilon$  for each kinetic energy outcome  $k$ , with probability of success  $> 95\%$ , it suffices to obtain

$$M \approx \frac{4\sigma^2(1 + (\eta - 1)\rho)}{\eta\epsilon^2} \leq \frac{1}{\epsilon^2} \quad (56)$$

many samples, where  $\epsilon$  controls the error between the estimator unbiased estimator  $\frac{1}{M} \sum_{i=1}^M T_i^{(k)}$  and the true mean  $\mathbb{E}[T^{(k)}]$ . This ensures that the empirical distribution over kinetic energies  $\hat{p}(k)$  and the true distribution over kinetic energies  $p(k)$  satisfies  $\max_k |\hat{p}(k) - p(k)| \leq \epsilon$ .

This completes the characterization of the cost to perform the photoemission spectrum algorithm. The cost for each subroutine is provided in Table I.

## V. APPLICATION: IMEPH RESOURCE ESTIMATION

In order to provide concrete estimates of the quantum simulation costs on fault tolerant quantum computers for the two physical quantities introduced above for EUV photolithography, we model a single molecule of 4-iodo-2-methylphenol as a representative monomer of a larger photoresist material, as shown in Figure 3. The inclusion of iodine is critical for resist performance, as its large cross-section at 92 eV dominates photon absorption compared to other halogenated materials [6]. By focusing on this single molecule model, we isolate the essential physics, specifically the excitation of iodine  $4d$  core states and the subsequent Auger decay cascade, that generates the low-energy electrons responsible for secondary electron effects. This reduction to a molecular Hamiltonian is physically justified by the ultrafast, localized nature of core-level relaxation, allowing us to tractably estimate the electronic dynamics while bypassing the computational complexity of simulating large bulk amorphous polymers.

### A. Absorption Sensitivity

First, we provide quantum resources estimates for computing the first quantity, absorption sensitivity of IMePh at 92 eV, using the approach de-

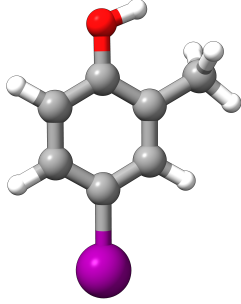


FIG. 3. Molecular structure of 4-iodo-2-methylphenol (IMePh). [51] White represents hydrogen atoms, grey for carbon, red for oxygen, and purple for iodine. For an all-electron representation of this system,  $\eta = 110$ .

scribed in Section III. We only consider logical qubit count and non-Clifford gate complexity throughout our resource estimation unless otherwise noted. A summary of the resource estimates can be found in Table II. The resource estimates in this table are computed following the approach described in section III.

The model system is constructed as follows: first, the Hartree-Fock orbitals for the IMePh molecular system were obtained in the def2-SVP basis set and corresponding effective core potential [52, 53]. Next, an active space was built using the automatic valence active spaces (AVAS) method at a threshold of 0.5. Two chemically inspired starting points were targeted: both included the I  $4d$  as well as the  $5s$  and  $5p$ , together with O  $2p$ . In addition, the first space included only the C  $2p_z$  orbitals, while the second included all C  $2p$  orbitals. Beyond that, larger active spaces with 40 and 50 orbitals were built by adding virtual orbitals to illustrate how slowly the cost grows with increasing active space size. All orbital computations and active space selections were computed using the PYSFCF software library [54–56]. Finally, within the active space chosen, compressed double factorization (CDF) of the 2-body interaction terms was introduced to reduce the overall cost of Hamiltonian simulation by this term into small fast forward-able fragments (this technique is sometimes also known as the Cartan subalgebra approach) [34–36], as already described in section III.

The main salient parameter determining the cost of the CDF is the number of fragments  $L$ : as reasonably well-established in the literature and following Ref. [24], we adopted  $L = N$  as sufficient to achieve our accuracy requirements. Other important parameters for cost estimation are the effective spectral norm of the Hamiltonian  $\|H\|_\omega$ , the truncation and discretization of the Fourier transform integral  $j_{\max}$

and  $\tau$ , respectively, the desired spectral resolution determined by the broadening  $\gamma$ , and finally the expected magnitude of the leading Trotter error term  $|\langle Y_3 \rangle|$ . We will determine many of these choices in a similar way as in Ref. [24].

For the spectral norm, looking to typical sizes of EUV spectra such as in Ref. [6] of around 120 eV, or roughly 4 Ha, we adopt  $\|H\|_\omega = 4$  Ha as a reasonable effective spectral range, and set  $\tau = \pi/2\|H\|_\omega$  as in Ref. [24]. Similarly, from that same data, a resolution of around  $\gamma = 1$  eV appears acceptable for the application goal of resolving the EUV absorption sensitivity, since the spectra do not appear to vary on a much shorter energy scale than this. As shown in Ref. [24],  $j_{\max} = O(\|H\|_\omega)$ : since in that work it was also found that  $j_{\max} = 100$  is more than sufficient for resolving features on the order of 1 eV with  $\|H\|_\omega = 2$ , here we adopt  $j_{\max} = 200$ . Finally, for the magnitude of the leading Trotter error  $|\langle Y_3 \rangle|$ , we raise the already conservative estimate of 1 Ha for 18 orbitals, and increase it by another order of magnitude to 10 Ha to accommodate the larger active spaces considered here. The dependence of the Trotter time step is square-root-like due to the expression  $\Delta = \sqrt{\gamma/|\langle Y_3 \rangle|}$ , so this amounts only to a modest increase to the total cost. Estimating Trotter error for these systems more firmly is an important extension that we leave to future work.

Finally, we incorporate the constant factors and shot count necessary for resolving the final absorption cross section value. As described above, the number of shots needed is

$$M = (\alpha\mathcal{N}\beta/\epsilon)^2. \quad (57)$$

To estimate the computational cost of simulating the absorption sensitivity of IMePh,  $\alpha = \frac{4\pi\omega}{3c}$  is photon frequency dependent prefactor, and we set the spectral bandwidth  $\gamma$  to be 2% of 92 eV, corresponding to experiment. The dipole normalization term,  $\mathcal{N} = \|D_\mu|\Phi\rangle\|$ , depends on a variety of factors, including the physical system size, basis set, etc. Using the Hartree-Fock ground state of IMePh over all orbitals in the def2-SVP basis, we compute the dipole normalization constant as 6.25 a.u. for the  $z$ -axis, 6.94 a.u. for the  $x$ -axis, and 6.84 a.u. for the  $y$ -axis respectively. For the resource estimates in Table II, we use a value of  $\mathcal{N} = 6.25$  for simplicity. Additionally, we target a loose screening precision of  $\epsilon = 0.1$ , providing a relative error of approximately 10% for strong absorbers. This threshold is likely sufficient to distinguish highly EUV sensitive materials from those that are not, but distinguishing two similarly sensitive materials would require a more accurate  $\epsilon$  error, and subsequently more shots.

TABLE II. **Absorption Sensitivity Resource Estimation.** The table lists the required number of logical qubits and maximum number of non-Clifford gates per circuit, and the total for varying active space sizes for computing the absorption sensitivity of IMePh at 92 eV using the algorithm in Section III for the IMePh molecule in the def2-SVP basis.

Number of Orbitals	Resource Estimates		
	Qubits	Gate Cost	Overall Cost
22	148	$3.94 \times 10^9$	$3.40 \times 10^{12}$
28	160	$8.14 \times 10^9$	$7.02 \times 10^{12}$
34	172	$1.46 \times 10^{10}$	$1.26 \times 10^{13}$
40	184	$2.38 \times 10^{10}$	$2.05 \times 10^{13}$
50	204	$4.65 \times 10^{10}$	$4.01 \times 10^{13}$

From these quantum resource estimations, we see that resolving the absorption sensitivity at a single frequency such as 92 eV is a low-medium cost quantum algorithm, with low logical qubit overhead. The maximum circuit sizes falling within the threshold of the capabilities of expected utility-scale fault-tolerant devices, but further optimizations will need to be made to make it viable for larger target monomers, such as tin-oxide materials.

### B. Photoemission Spectra

Second, we then compute resource estimates for the photoemission simulation algorithm for IMePh, using the first quantized approach in Section IV. Similar to the previous subsection, we report logical qubit counts, as well the total number of non-Clifford gates to compute the target quantity.

For the results presented in this subsection, the simulation cell cubic box length has a size of  $\Omega^{1/3} = 200$  Bohr, 10x the length of the longest side length of the IMePh molecule. Additionally, the state preparation cost from Section IV C 1 is estimated using the `orb2mps-fq` software library [43] using the IMePh molecule in an all-electron STO-3G basis set. The choice of the minimal STO-3G basis is justified by recognizing that the MPS based orbital state preparation method is dominated by costly representations of the “sharpness” of core orbitals in real-space, in this case, the iodine 1s orbital. The cost of the state-*prep* then relies solely on the number of electrons, or orbitals included and the spatial distribution of the 1s orbital.

Additionally for this calculation, the MPS optimized basis transform from Gaussians to plane waves for each molecular orbital was ensured to have a fidelity of  $\geq 0.99$ , the SVD cutoff used was  $10^{-3}$ , and the non-Clifford gate count was computed using Eq. (F94) of Ref. [43] for each MPS orbital representa-

tion, and the rotation error in the synthesis was set to  $10^{-4}$ . Overall, this state-preparation cost for all occupied orbitals is  $\sim 10^9$  non-Clifford gates, orders of magnitude lower than the Hamiltonian simulation cost in the grand total.

A summary of the resource estimates can be found in Table III for the all-electron system. Additionally, for the following results, we assume that we can reduce the number of electrons in the simulation from the all electron approach at  $\eta = 110$ , down to  $\eta = 58$ , using pseudopotential based methods. This reduction in electron count is detailed in Appendix B. Pseudopotential based methods slightly modify the electron-nuclear interaction term, freeze out core electrons, and reduce the overall cost of the algorithm. Details of this modification are detailed in App. C. The costs of both models are reported for completeness.

From these results, we see that while the real-time evolution of the physical process we are simulating is small ( $\sim 1 - 10$  fs) due to the ultrafast nature of Auger decay, the overhead in the gate costs driving up the number of non-Clifford gates is primarily due to the one-norm of the first quantized Hamiltonian in qubitized time evolution. Some of this cost is mitigated by using a pseudopotential approach, and reducing the total electrons in the system, but the overheads remain costly. Additionally, the logical qubit count is moderate, on the order of 1000s.

## VI. CONCLUSION AND FUTURE WORK

In this work, we have introduced two new quantum simulation algorithms to address critical material design challenges facing Extreme Ultraviolet (EUV) lithography. As the semiconductor industry pushes toward smaller and smaller features on the atomic scale, the line edge roughness and blur driven by secondary electron cascades induced by

TABLE III. **Photoemission Spectrum Resource Estimation** The table lists the required logical qubits and non-Clifford gate counts for varying the planewave grid size and simulation times for the approach introduced in Section IV. We compare both the all electron (AE) method and pseudopotential (PP). These numbers use a computational volume of  $\Omega = 200\text{\AA}^3$ , and are reported assuming that the success probability of applying the dipole operator and window function  $P_d = 10^{-3} = P_w$ , and that  $P_c = 1$ . The gate cost reflects the number of non-Clifford gates in any individual circuit, and the overall cost includes the sampling complexity of repeating each circuit  $1/\epsilon^2$  times with  $\epsilon = 0.01$ . The number of planewave modes for AE and PP is reflective of the fidelity each method provides in terms of representing the ground state wavefunction in a second quantized basis. The first AE and PP rows show the cost to provide  $> 10\%$  fidelity, the second  $> 70\%$  fidelity, and the final rows to  $> 99\%$  fidelity with the second quantized ground state. We observe that in all instances PP uses significantly fewer overall qubits, but for larger numbers of planewaves has a gate cost that is slightly larger than, but comparable to, the AE cases for similar fidelity.

Simulation Parameters			Resource Estimates		
Method	Basis Size	Time (fs)	Qubits	Gate Cost	Overall Cost
AE	$N_{pw}^{1/3} = 2^9$	1	4544	$3.49 \times 10^{14}$	$3.49 \times 10^{18}$
		10	4544	$3.65 \times 10^{14}$	$3.65 \times 10^{18}$
AE	$N_{pw}^{1/3} = 2^{11}$	1	5668	$1.73 \times 10^{15}$	$1.73 \times 10^{19}$
		10	5668	$1.81 \times 10^{15}$	$1.81 \times 10^{19}$
AE	$N_{pw}^{1/3} = 2^{13}$	1	6848	$8.32 \times 10^{15}$	$8.32 \times 10^{19}$
		10	6848	$8.69 \times 10^{15}$	$8.69 \times 10^{19}$
PP	$N_{pw}^{1/3} = 2^6$	1	2212	$4.74 \times 10^{13}$	$4.74 \times 10^{17}$
		10	2212	$4.94 \times 10^{13}$	$4.94 \times 10^{17}$
PP	$N_{pw}^{1/3} = 2^8$	1	3192	$2.97 \times 10^{15}$	$2.97 \times 10^{19}$
		10	3192	$3.10 \times 10^{15}$	$3.10 \times 10^{19}$
PP	$N_{pw}^{1/3} = 2^9$	1	3549	$4.11 \times 10^{16}$	$4.11 \times 10^{20}$
		10	3549	$4.30 \times 10^{16}$	$4.30 \times 10^{20}$

EUV photons has emerged as a fundamental bottleneck limiting the further reduction of transistor size, and is difficult to computational model accurately. The quantum simulations proposed here and the subsequent observables, serve as high-fidelity parameterization inputs for broader multi-scale models that use molecular dynamics, kinetic Monte Carlo methods, and more. By providing accurate *ab initio* data for the absorption sensitivity and the Auger spectrum of ejected electrons, these quantum simulations enable better calibration of macroscopic exposure models that are otherwise limited by the accuracy of their underlying parameters.

To address these key parameters, we developed two distinct simulation protocols targeting the primary mechanisms of EUV exposure. First, we presented a coherent time-domain algorithm to compute the absorption cross-section specifically at the 92 eV operating frequency. By bypassing full spectrum algorithmic approach in favor of a more targeted dipole autocorrelation function, we demonstrated that candidate monomers like 4-iodo-2-methylphenol (IMePh) can be screened with relatively low quantum resources, estimated at fewer than 200 logical qubits with costs per circuit of  $10^9$  total non-Clifford gates and approximately  $10^3$  shots

for the smallest instance. Second, we addressed the complex electron dynamics of Auger decay and photoelectron emission by utilizing a first-quantized planewave basis representation. This approach, coupled with a novel dipole energy windowing, and real-space projection operator to distinguish bound versus continuum states, allows for the rigorous sampling of the ejected electron’s kinetic energy spectrum. The total cost of this novel algorithm is currently still high for reasonably sized grid spacings,  $\geq 10^{13}$  total non-Clifford gates per circuit and  $10^4$  shots, but the logical qubit count is moderate, on the order of  $10^3$ .

Future work will focus on optimizing the algorithmic primitives identified as the primary computational bottlenecks in this study. Specifically, the cost of the photoelectron emission simulation is currently dominated by the extensive gate overhead required for Hamiltonian time evolution in the first-quantized basis. Research into hybrid basis representations could significantly reduce the circuit depth required to propagate the wavefunction into the ionization continuum. Additionally, the direct integration of these quantum simulated Auger spectra into classical Monte Carlo electron-scattering models remains a key objective, connecting atomic-scale quantum

dynamics and the predictive quantification of photoresist blur.

### ACKNOWLEDGMENTS

We thank Tarik El-Khateeb for assistance with creating Fig. 1, and Alexander Kunitsa for early feedback and helpful discussions.

- 
- [1] T. Kozawa and S. Tagawa, Radiation chemistry in chemically amplified resists, *Japanese Journal of Applied Physics* **49**, 030001 (2010).
- [2] D. F. Ogletree, Molecular excitation and relaxation of extreme ultraviolet lithography photoresists, in *Frontiers of Nanoscience*, Vol. 11 (Elsevier, 2016) pp. 91–113.
- [3] J. H. Ma, H. Wang, D. Prendergast, A. Neureuther, and P. Naulleau, Investigating extreme ultraviolet radiation chemistry with first-principles quantum chemistry calculations, *Journal of Micro/Nanolithography, MEMS, and MOEMS* **19**, 034601 (2020).
- [4] M. Kim, J. Moon, J. Choi, S. Park, B. Lee, and M. Cho, Multiscale simulation approach on sub-10 nm extreme ultraviolet photoresist patterning: Insights from nanoscale heterogeneity of polymer, *Macromolecules* **51**, 6922 (2018).
- [5] H. Lee, S. Park, M. Kim, J. Moon, B. Lee, and M. Cho, Multiscale simulation of extreme ultraviolet nanolithography: impact of acid–base reaction on pattern roughness, *Journal of Materials Chemistry C* **9**, 1183 (2021).
- [6] K. D. Closser, D. F. Ogletree, P. Naulleau, and D. Prendergast, The importance of inner-shell electronic structure for enhancing the euv absorption of photoresist materials, *The Journal of Chemical Physics* **146** (2017).
- [7] S. Fomichev, K. Hejazi, I. Loaiza, M. S. Zini, A. Delgado, A.-C. Voigt, J. E. Mueller, and J. M. Arrazola, Simulating x-ray absorption spectroscopy of battery materials on a quantum computer, arXiv preprint arXiv:2405.11015 (2024).
- [8] T. Kharazi, T. F. Stetina, L. Ko, G. H. Low, and K. B. Whaley, An efficient quantum algorithm for generation of ab initio n-th order susceptibilities for non-linear spectroscopies, arXiv preprint arXiv:2404.01454 (2024).
- [9] O. Kostko, B. Xu, M. Ahmed, D. S. Slaughter, D. F. Ogletree, K. D. Closser, D. G. Prendergast, P. Naulleau, D. L. Olynick, P. D. Ashby, *et al.*, Fundamental understanding of chemical processes in extreme ultraviolet resist materials, *The Journal of chemical physics* **149** (2018).
- [10] L. Fernández Míguez, P. Bobbert, and R. Coehoorn, Molecular-scale kinetic monte carlo simulation of pattern formation in photoresist materials for euv nanolithography, *Journal of Applied Physics* **136** (2024).
- [11] P. L. Theofanis, J. M. Blackwell, M. E. Krysak, and F. Gstrein, Modeling photon, electron, and chemical interactions in a model hafnium oxide nanocluster euv photoresist, in *Extreme Ultraviolet (EUV) Lithography XI*, Vol. 11323 (SPIE, 2020) pp. 92–105.
- [12] W. Skomorowski and A. I. Krylov, Feshbach–fano approach for calculation of auger decay rates using equation-of-motion coupled-cluster wave functions. ii. numerical examples and benchmarks, *The Journal of chemical physics* **154** (2021).
- [13] F. Matz and T.-C. Jagau, Molecular auger decay rates from complex-variable coupled-cluster theory, *The Journal of Chemical Physics* **156** (2022).
- [14] N. K. Jayadev, A. Ferino-Pérez, F. Matz, A. I. Krylov, and T.-C. Jagau, The auger spectrum of benzene, *The Journal of Chemical Physics* **158** (2023).
- [15] P. Burke, C. Noble, and V. Burke, R-matrix theory of atomic, molecular and optical processes, *Advances In Atomic, Molecular, and Optical Physics* **54**, 237 (2007).
- [16] P. Descouvemont and D. Baye, The r-matrix theory, *Reports on progress in physics* **73**, 036301 (2010).
- [17] A. C. Brown, G. S. Armstrong, J. Benda, D. D. Clarke, J. Wragg, K. R. Hamilton, Z. Mašín, J. D. Gorfinkiel, and H. W. van der Hart, Rmt: R-matrix with time-dependence. solving the semi-relativistic, time-dependent schrödinger equation for general, multielectron atoms and molecules in intense, ultrashort, arbitrarily polarized laser pulses, *Computer Physics Communications* **250**, 107062 (2020).
- [18] Z. Mašín, J. Benda, J. D. Gorfinkiel, A. G. Harvey, and J. Tennyson, Ukmol+: A suite for modelling electronic processes in molecules interacting with electrons, positrons and photons using the r-matrix method, *Computer Physics Communications* **249**, 107092 (2020).
- [19] F. Covito, E. Perfetto, A. Rubio, and G. Stefanucci, Real-time dynamics of auger wave packets and decays in ultrafast charge migration processes, *Physical Review A* **97**, 061401 (2018).
- [20] F. Covito, E. Perfetto, A. Rubio, and G. Stefanucci, Benchmarking nonequilibrium green’s functions against configuration interaction for time-dependent auger decay processes, *The European Physical Journal B* **91**, 216 (2018).
- [21] T. Åberg and G. Howat, *Theory of the Auger effect*, Vol. 6 (1982).
- [22] W. P. Reinhardt, Complex coordinates in the theory of atomic and molecular structure and dynamics, *Annual Review of Physical Chemistry* **33**, 223 (1982).
- [23] T.-C. Jagau, Theory of electronic resonances: fundamental aspects and recent advances, *Chemical Communications* **58**, 5205 (2022).
- [24] S. Fomichev, P. A. Casares, J. Soni, U. Azad, A. Kunitsa, A.-C. Voigt, J. E. Mueller, and J. M. Arrazola, Fast simulations of x-ray absorption spectroscopy for battery materials on a quantum computer, arXiv

- preprint arXiv:2506.15784 (2025).
- [25] A. Kunitsa, D. Dhawan, S. Fomichev, J. M. Arrazola, M. Zhang, and T. F. Stetina, Quantum simulation of electron energy loss spectroscopy for battery materials, arXiv preprint arXiv:2508.15935 (2025).
- [26] Y. Zhou, P. A. Casares, D. Dhawan, I. Loaiza, S. Jahangiri, R. A. Lang, J. M. Arrazola, and S. Fomichev, Quantum algorithms for photoreactivity in cancer-targeted photosensitizers, arXiv preprint arXiv:2512.15889 (2025).
- [27] L. Lin and Y. Tong, Heisenberg-Limited Ground-State Energy Estimation for Early Fault-Tolerant Quantum Computers, PRX Quantum **3**, 010318 (2022).
- [28] D. Motlagh and N. Wiebe, Generalized quantum signal processing, PRX Quantum **5**, 020368 (2024).
- [29] S. Fomichev, K. Hejazi, M. S. Zini, M. Kiser, J. Fraxanet, P. A. M. Casares, A. Delgado, J. Huh, A.-C. Voigt, J. E. Mueller, *et al.*, Initial state preparation for quantum chemistry on quantum computers, PRX Quantum **5**, 040339 (2024).
- [30] S. R. White, Density matrix formulation for quantum renormalization groups, Physical review letters **69**, 2863 (1992).
- [31] G. K.-L. Chan and M. Head-Gordon, Highly correlated calculations with a polynomial cost algorithm: A study of the density matrix renormalization group, The Journal of chemical physics **116**, 4462 (2002).
- [32] C. F. Bender and E. R. Davidson, Studies in configuration interaction: The first-row diatomic hydrides, Physical Review **183**, 23 (1969).
- [33] J. Whitten and M. Hackmeyer, Configuration interaction studies of ground and excited states of polyatomic molecules. i. the ci formulation and studies of formaldehyde, The Journal of Chemical Physics **51**, 5584 (1969).
- [34] J. Cohn, M. Motta, and R. M. Parrish, Quantum filter diagonalization with compressed double-factorized hamiltonians, PRX Quantum **2**, 040352 (2021).
- [35] T.-C. Yen and A. F. Izmaylov, Cartan subalgebra approach to efficient measurements of quantum observables, PRX quantum **2**, 040320 (2021).
- [36] O. Oumarou, M. Scheurer, R. M. Parrish, E. G. Hohenstein, and C. Gogolin, Accelerating quantum computations of chemistry through regularized compressed double factorization, Quantum **8**, 1371 (2024).
- [37] I. D. Kivlichan, J. McClean, N. Wiebe, C. Gidney, A. Aspuru-Guzik, G. K.-L. Chan, and R. Babbush, Quantum simulation of electronic structure with linear depth and connectivity, Physical Review Letters **120**, 110501 (2018).
- [38] D. J. Thouless, Stability conditions and nuclear rotations in the hartree-fock theory, Nuclear Physics **21**, 225 (1960).
- [39] J. M. Arrazola, O. Di Matteo, N. Quesada, S. Jahangiri, A. Delgado, and N. Killoran, Universal quantum circuits for quantum chemistry, Quantum **6**, 742 (2022).
- [40] S. G. Mehendale, L. A. Martínez-Martínez, P. D. Kamath, and A. F. Izmaylov, Estimating trotter approximation errors to optimize hamiltonian partitioning for lower eigenvalue errors, arXiv preprint arXiv:2312.13282 (2023).
- [41] N. Lin, Y. Chen, X. Wei, W. Yang, and Y. Leng, Spectral purity systems applied for laser-produced plasma extreme ultraviolet lithography sources: a review, High Power Laser Science and Engineering **11**, e64 (2023).
- [42] Y. Su, D. W. Berry, N. Wiebe, N. Rubin, and R. Babbush, Fault-Tolerant Quantum Simulations of Chemistry in First Quantization, PRX Quantum **2**, 1 (2021), arXiv: 2105.12767v2 ISBN: 2105.12767v3.
- [43] W. J. Huggins, O. Leimkuhler, T. F. Stetina, and K. B. Whaley, Efficient state preparation for the quantum simulation of molecules in first quantization, PRX Quantum **6**, 020319 (2025).
- [44] R. Babbush, W. J. Huggins, D. W. Berry, S. F. Ung, A. Zhao, D. R. Reichman, H. Neven, A. D. Baczewski, and J. Lee, Quantum simulation of exact electron dynamics can be more efficient than classical mean-field methods, Nature Communications **14**, 4058 (2023).
- [45] G. H. Low and I. L. Chuang, Optimal hamiltonian simulation by quantum signal processing, Phys. Rev. Lett. **118**, 010501 (2017).
- [46] A. Gilyén, Y. Su, G. H. Low, and N. Wiebe, Quantum singular value transformation and beyond: exponential improvements for quantum matrix arithmetics, in *Proceedings of the 51st Annual ACM SIGACT Symposium on Theory of Computing* (2019) pp. 193–204, arXiv:1806.01838 [quant-ph].
- [47] Y. R. Sanders, G. H. Low, A. Scherer, and D. W. Berry, Black-box quantum state preparation without arithmetic, Phys. Rev. Lett. **122**, 020502 (2019).
- [48] C. Gidney, Halving the cost of quantum addition, Quantum **2**, 74 (2018), arXiv:1709.06648 [quant-ph].
- [49] G. H. Low and I. L. Chuang, Hamiltonian Simulation by Qubitization, Quantum **3**, 163 (2019).
- [50] U. De Giovannini, D. Varsano, M. A. Marques, H. Appel, E. K. Gross, and A. Rubio, Ab initio angle-and energy-resolved photoelectron spectroscopy with time-dependent density-functional theory, Physical Review A—Atomic, Molecular, and Optical Physics **85**, 062515 (2012).
- [51] National Center for Biotechnology Information, PubChem Compound Summary for CID 143713, 4-Iodo-2-methylphenol (2025), retrieved December 16, 2025.
- [52] K. A. Peterson, D. Figgen, E. Goll, H. Stoll, and M. Dolg, Systematically convergent basis sets with relativistic pseudopotentials. ii. small-core pseudopotentials and correlation consistent basis sets for the post-d group 16-18 elements, J. Chem. Phys. **119**, 11113 (2003).
- [53] F. Weigend and R. Ahlrichs, Balanced basis sets of split valence, triple zeta valence and quadruple zeta valence quality for h to rn: Design and assessment of

- accuracy, Phys. Chem. Chem. Phys. **7**, 3297 (2005).
- [54] Q. Sun, Libcint: An efficient general integral library for gaussian basis functions, Journal of computational chemistry **36**, 1664 (2015).
- [55] Q. Sun, T. C. Berkelbach, N. S. Blunt, G. H. Booth, S. Guo, Z. Li, J. Liu, J. D. McClain, E. R. Sayfutyarova, S. Sharma, *et al.*, Pyscf: the python-based simulations of chemistry framework, Wiley Interdisciplinary Reviews: Computational Molecular Science **8**, e1340 (2018).
- [56] Q. Sun, X. Zhang, S. Banerjee, P. Bao, M. Barbry, N. S. Blunt, N. A. Bogdanov, G. H. Booth, J. Chen, Z.-H. Cui, *et al.*, Recent developments in the pyscf program package, The Journal of chemical physics **153** (2020).
- [57] Y. R. Sanders, D. W. Berry, P. C. Costa, L. W. Tessler, N. Wiebe, C. Gidney, H. Neven, and R. Babbush, Compilation of Fault-Tolerant Quantum Heuristics for Combinatorial Optimization, PRX Quantum **1**, 020312 (2020).
- [58] M. S. Zini, A. Delgado, R. d. Reis, P. A. M. Casares, J. E. Mueller, A.-C. Voigt, and J. M. Arrazola, Quantum simulation of battery materials using ionic pseudopotentials, Quantum **7**, 1049 (2023), arXiv:2302.07981 [quant-ph].
- [59] X.-R. D. Booklet, X-ray data booklet, Laboratory, Univ. California , 1 (2001).
- [60] C. Hartwigsen, S. Goedecker, and J. Hutter, Relativistic separable dual-space gaussian pseudopotentials from h to rn, Physical Review B **58**, 3641 (1998).
- [61] M. J. Van Setten, M. Giantomassi, E. Bousquet, M. J. Verstraete, D. R. Hamann, X. Gonze, and G.-M. Rignanese, The pseudodojo: Training and grading a 85 element optimized norm-conserving pseudopotential table, Computer Physics Communications **226**, 39 (2018).
- [62] M. L. Urquiza, M. Gatti, and F. Sottile, Pseudopotential bethe-salpeter calculations for shallow-core x-ray absorption near-edge structures: Excitonic effects in  $\alpha$ -al 2 o 3, Physical Review B **107**, 205148 (2023).
- [63] M. S. Zini, A. Delgado, R. dos Reis, P. A. M. Casares, J. E. Mueller, A.-C. Voigt, and J. M. Arrazola, Quantum simulation of battery materials using ionic pseudopotentials, Quantum **7**, 1049 (2023).

## Appendix A: Quantum subroutines

### 1. Block Encoding

Block encoding is a ubiquitous protocol for implementing linear, but not necessarily unitary, operations on a quantum computer. A block encoding of a matrix  $A$  can be implemented as a unitary  $U_A$  by encoding the action of  $A$  within a block of  $U_A$ . The block encoding is characterized by 3 parameters,  $\alpha$  the subnormalization factor which ensures that  $\|A\|/\alpha \leq 1$ ,  $m$  the number of ancilla qubits used to flag the successful application of  $A/\alpha$ , and  $\epsilon$  which bounds the error between the desired operation and the block encoded matrix. The above are codified into the following definition.

**Definition 1** ( $(\alpha, m, \epsilon)$ -BE( $A$ )). *Let  $A$  be a matrix operating on  $n$  qubits. We say that a unitary matrix  $U_A$  is an  $(\alpha, m, \epsilon)$ -BE( $A$ ) if*

$$\|(I_{2^n} \otimes \langle 0_m |) \alpha U_A (I_{2^n} \otimes |0_m \rangle) - A\| \leq \epsilon, \quad (\text{A1})$$

where  $|0_m \rangle$  is the  $m$  qubit all-zero state.

A characterization of a block encoding at the operational level is that

$$U_A : |\psi \rangle |0_m \rangle \rightarrow \frac{A}{\alpha} |\psi \rangle |0_m \rangle + |\perp \rangle$$

where  $|\perp \rangle$  is some unnormalized quantum state perpendicular to  $|\psi \rangle |0_m \rangle$ .

Throughout this work, we will employ the linear combination of unitaries (LCU) method to construct block encodings. As the name suggests, we write the block encoded matrix  $A$  in terms of a linear combination of unitary matrices  $U_l$ , with coefficients  $c_l$ , i.e.  $A = \sum_{l=0}^{M-1} c_l U_l$ , where  $m = \lceil \log(M) \rceil$ . Without loss of generality, we may assume that the coefficients  $c_l$  are positive. The subnormalization factor for the LCU approach is given by the 1-norm of the coefficients  $\alpha = \sum_{l=0}^{M-1} |c_l|$ . The LCU method consists of two subroutines

$$\begin{aligned} \text{PREPARE} : |0_m \rangle &\rightarrow \sum_{l=0}^{M-1} \sqrt{\frac{c_l}{\alpha}} |l_m \rangle \\ \text{SELECT} &= \sum_{l=0}^{M-1} U_l \otimes |l_m \rangle \langle l_m|, \end{aligned} \quad (\text{A2})$$

consisting of a state preparation protocol on the ancilla PREPARE and controlled the application of the  $U_l$  in SELECT. The block encoding  $U_A$  obtained via block encoding is

$$U_A = \text{PREPARE}^\dagger \cdot \text{SELECT} \cdot \text{PREPARE}. \quad (\text{A3})$$

## 2. Inequality Testing

A common technique in this work, as well as that used in the block encoding construction of the electronic Hamiltonian, is that of *inequality testing*. This technique was first introduced in Ref. [47], and has been fruitfully employed to improve the efficiency of many quantum subroutines [42, 57, 58]. The main innovation of the inequality test is the subroutine

$$\text{COMP} : |\alpha\rangle_n |\beta\rangle_n |0\rangle \rightarrow |\alpha\rangle_n |\beta\rangle_n |b(\beta < \alpha)\rangle,$$

where  $b(x)$  is a Boolean function. The implementation of the comp subroutine is simple, we just perform a subtraction circuit which requires only  $n$  Toffoli gates. For our work, this subroutine naturally produces a block encoding of the position operator, since for any  $\alpha \in \{0, \dots, 2^n - 1\}$  we have

$$\begin{aligned} |\alpha\rangle_n |0\rangle_n |0\rangle &\xrightarrow{\text{UNIF}} \frac{1}{\sqrt{2^n}} \sum_{\beta=0}^{2^n-1} |\alpha\rangle_n |\beta\rangle_n |0\rangle \\ &\xrightarrow{\text{COMP}} \frac{1}{\sqrt{2^n}} \sum_{\beta=0}^{2^n-1} |\alpha\rangle_n |\beta\rangle_n |b(\beta < \alpha)\rangle \\ &= \frac{1}{\sqrt{2^n}} \left( \sum_{\beta < \alpha} |\alpha\rangle_n |\beta\rangle_n |0\rangle + \sum_{\beta > \alpha} |\alpha\rangle_n |\beta\rangle_n |1\rangle \right) \\ &\xrightarrow{\text{UNIF}^\dagger} \frac{1}{2^n} |\alpha\rangle_n |0\rangle_n \left( |0\rangle \sum_{0 \leq x \leq \alpha-1} + |1\rangle \sum_{\alpha-1 \leq x \leq 2^n-1} \right) \\ &= \frac{\alpha}{2^n} |\alpha\rangle_n |0\rangle_n |0\rangle + \frac{2^n - \alpha}{2^n} |\alpha\rangle_n |0\rangle_n |1\rangle. \end{aligned}$$

Since the quantum states are encoded with signed integers, we would just need to apply a Pauli Z controlled on the sign bit to get the signed position operator we use.

The inequality testing protocol can be extended to compute more complex functions as well. For the projector onto the continuum states, we need to test if  $\|q_i\| \leq R_c$ . Since  $R_c$  is a fixed constant, we do not need to load it into memory. Since the values stored in binary are the indexes to the positions in real space, we need to scale the radius by the lattice spacing  $h = \frac{N^{1/3}}{\Omega^{1/3}}$ , and compute a binary representation of  $\left(\frac{R_c}{h}\right)^2$ . Now our goal is to determine if the inequality

$$\|q_i\|^2 \leq \left(\frac{R_c}{h}\right)^2$$

on the quantum computer. We can do this by first computing  $\|q_i\|^2$  in binary, and replacing COMP with a subtraction by classical constant circuit, which we will denote as  $\text{COMP}_c$ . The operations on the quantum computer are as follows

$$\begin{aligned} |q_x\rangle |q_y\rangle |q_z\rangle |0\rangle |0\rangle &\xrightarrow{\text{SUM-SQUARES}} |q_x\rangle |q_y\rangle |q_z\rangle \|\|q\|^2\rangle |0\rangle \\ &\xrightarrow{\text{COMP}_c} |q_x\rangle |q_y\rangle |q_z\rangle \|\|q\|^2\rangle |b(\|\|q\|^2 \leq R^2)\rangle, \end{aligned}$$

and uncomputing the subtraction by classical constant and sum-of-squares circuits, we obtain the state

$$|q_x\rangle |q_y\rangle |q_z\rangle |0\rangle |b(\|\|q\|^2 \leq R^2)\rangle,$$

which provides a single qubit flag denoting the status of the inequality test.

This technique is particularly powerful when combined with the construction of Ref. [48]. This paper introduces a technique called “measure and fixup”, which replaces Toffolis used in the uncomputation of a circuit with a measurement and a controlled single qubit Pauli  $Z$  operation. Thus, the circuits for squaring, COMP, and other arithmetic circuits can be uncomputed with zero non-Clifford cost, essentially halving the overall cost of the subroutine.

## Appendix B: BE of FQ Hamiltonian

The block encoding of the first quantized plane wave Hamiltonian was described in great detail in Ref. [42]. We review the main subroutines and costs associated with constructing this block encoding. First, we provide a restatement of Theorem 4 of Ref. [42], which gives the overall Toffoli gate cost to perform the block encoding.

**Theorem 1** (Resource estimate to block encode  $H$ ). *Let  $H$  be the electronic Hamiltonian describing a system of  $\eta$  electrons occupying positions in a domain  $\Omega \subset \mathbb{R}^3$ , discretized using  $N^{1/3} \in \mathbb{N}$  plane waves per degree of freedom. Let  $n = \lceil \log(N^{1/3}) \rceil$  be the number of qubits per degree of freedom, for a total of  $3\eta n$  qubits to describe all of the system degrees of freedom. Then, using the methods described in Ref. [42], one can obtain an  $(\lambda, n_{\text{ref}}, \epsilon)$ -BE( $H$ ) where*

$$\lambda = \max\left\{\lambda'_T + \lambda_U + \lambda_V, \frac{\lambda_U + \lambda_V(1 - \eta^{-1})^{-1}}{p_\nu}\right\} \quad (\text{B1})$$

$$n_{\text{ref}} = 3n^2 + 4n_M(n + 1) + 6n + 5 + \max\{n_T, n_R + 1\},$$

and  $p_\nu$  is the probability of preparing the momentum state  $\sum_{\nu \in G_0} \frac{1}{\|\nu\|} |\nu\rangle$ , and  $\lambda'_T = \frac{6\eta\pi^2}{\Omega^{2/3}} 2^{2(n-1)}$ . With  $n_T$ ,  $n_R$ ,  $n_M$  chosen according to

$$\begin{aligned} \epsilon_M &= \frac{2\eta}{2^{n_M} \pi \Omega^{1/3}} (\eta - 1 + 2\lambda_\zeta) \\ \epsilon_R &= \frac{\eta \lambda_\zeta}{2^{n_R} \Omega^{1/3}} \sum_{\nu \in G_0} \frac{1}{\|\nu\|} \\ \epsilon_T &= \frac{\pi \lambda}{2^{n_T}}, \end{aligned} \quad (\text{B2})$$

so that overall

$$(\epsilon_M + \epsilon_R + \epsilon_T)^2 < \epsilon^2. \quad (\text{B3})$$

Moreover, this block encoding is accomplished using

$$n_M + 6n + 2n_\eta + n_{\eta\zeta} + \max\{5n_R - 4, 5n + 1\} + 18 \quad (\text{B4})$$

ancilla qubits in addition to  $n_r$ . The Toffoli cost to perform one query to the qubitized block encoding is

$$\begin{aligned} &2(n_T + 4n_{\eta\zeta} + 2b_r - 12) + 14n_\eta + 8b_r - 36 + 12\eta n + 4\eta - 8 + 5(n - 1) + 2 + \\ &3n^2 + 15n + 4n_M(n + 1) - 7 + \lambda_\zeta + 24n + 3(2n n_R - n(n + 1) - 1). \end{aligned} \quad (\text{B5})$$

**Corollary 1** (Block encoding of IMePh Hamiltonian). *The IMePh molecule has  $\eta = 110$  electrons and  $\lambda_\zeta = 110$ . Choosing a side length  $\Omega^{1/3}$  to be  $\sim 10\times$  the length of longest side of the molecule side gives  $\Omega^{1/3} = 200 \text{ \AA}$ . The kinetic energy of a grid of  $N^{1/3}$  points per dimension can represent a kinetic energy  $E_{\text{cut}} = \frac{1}{2} \frac{N^{2/3}}{\Omega^{2/3}}$ . Since the 1s orbital of Iodine has kinetic energy of  $\sim 1215 \text{ Ha}$ , we can safely assume that the largest kinetic energy of the molecule  $T_{\text{max}} < \eta \times 1215 \text{ Ha}$ . Therefore, we may choose a number of grid points*

$$N^{1/3} \geq \frac{200}{\pi} \sqrt{\frac{2 \times 110 \times 1215}{3}} \sim 1.9 \times 10^4, \quad (\text{B6})$$

Quantities characterizing Hamiltonian block encoding costs		
Symbol	Scaling	Description
$N$	$\Omega k_{\max}^{3/2}$	Number of plane wave modes per electron
$\Omega$	Problem dependent ( $200^3 \text{\AA}^3$ here)	The volume of the computational region
$n_M$	$\log\left(\frac{4\eta^2}{\Omega^{1/3}}\right)$	Number of ancilla qubits in inequality testing for preparation of Coulomb potential
$n_R$	$\log(\lambda_U)$	Number of ancilla qubits to encode nuclear coordinates in binary
$n_T$	$\log(\lambda)$	The number of ancilla qubits used to encode the coefficient selecting between $T$ and $U + V$
$n_\eta$	$\log(\eta)$	Number of ancilla qubits to encode $\eta$ degrees of freedom
$n_{\eta\zeta}$	$\log(\eta + 2\lambda_\zeta)$	Number of ancilla qubits to encode $\eta + 2\lambda_\zeta$ degrees of freedom
$b_r$	$O(1)$	Number of bits of precision in rotation angle for preparing equal superposition state
$\lambda_\zeta$	$\sum_{j=0}^{L-1}  \zeta_j $	One norm of nuclear charges
$\lambda_T$	$6\eta\pi^2 \frac{N^{2/3}}{\Omega^{2/3}}$	Subnormalization factor for the kinetic energy term
$\lambda_U$	$\eta\lambda_\zeta \frac{N^{1/3}}{\Omega^{1/3}}$	Subnormalization factor for nuclear-electron interaction
$\lambda_V$	$\eta^2 \frac{N^{1/3}}{\Omega^{1/3}}$	Subnormalization factor for electron-electron interaction

TABLE IV. The quantities characterizing the costs in the block encoding of the electronic Hamiltonian, under Born-Oppenheimer approximation, in a first quantized plane wave basis.

and

$$n = \lceil \log(N^{1/3}) \rceil = 15 \quad (\text{B7})$$

qubits to represent each degree of freedom. Therefore, we require  $3n\eta = 4950$  qubits to represent the system. The one norms of the relative terms are

$$\begin{aligned} \lambda'_T &= 4.37 \times 10^7 \\ \lambda_U &= 7.5 \times 10^6 \\ \lambda_V &= 1.23 \times 10^7 \end{aligned} \quad (\text{B8})$$

and find that  $P_{eq} \sim 1$ , and the overall subnormalization factor is

$$\lambda \sim 5.00 \times 10^7. \quad (\text{B9})$$

Taking the overall  $\epsilon = .5\epsilon_{chem} \sim 8 \times 10^{-4} \text{Ha}$ , and taking the choice of  $\epsilon_T = \epsilon_R = \epsilon_M = \epsilon/3$ , gives

$$\begin{aligned} n_M &= 36 \\ n_R &= 50 \\ n_T &= 35. \end{aligned} \quad (\text{B10})$$

Therefore, the total number of Toffoli gates to perform one query of the block encoding is

$$T_1 = 2.53 \times 10^4, \quad (\text{B11})$$

and the number of ancilla qubits is

$$q_{anc} = 3542, \quad (\text{B12})$$

for a total of

$$q_{tot} = 8084 \quad (\text{B13})$$

logical qubits in the simulation.

### Appendix C: Pseudopotential modified FQ method

While pseudopotential usage is rapidly becoming routine in quantum algorithms, it is still a highly demanding task to re-build a given algorithm with pseudopotentials in mind. In this manuscript, we aim to only obtain a rough estimate of the cost reduction to be expected from the use of pseudopotentials as opposed to all-electron calculations, and reserve the full derivation of the implementation of the pseudopotential for this case to a follow-up work.

The basic motivation to use pseudopotentials is that EUV light with 92 eV energy will not excite deep-core electrons, so they might as well be frozen out in the pseudopotential. However, care needs to be taken with this, because EUV light will excite shallow-core (or semi-core) electrons, unlike what happens in, for example, UVvis spectroscopy. For the IMePh molecule with iodine, formal valence counting suggests that the iodine valence orbitals are the 5s and 5p, leaving only 7 valence electrons outside the core: however, it is well-known that the semi-core 4d orbitals play a key role in EUV absorption [6]. This can be gleaned from the fact that the 4d (atomic-like) binding energies are around 50 eV based on tabulated X-ray excitation data [59], so they can easily be excited by EUV at 92 eV. By contrast, the next-deepest levels of 4s/4p have binding energies in excess of 120 eV, so these and deeper levels can likely be frozen out.

The challenge is that most standard pseudopotentials for iodine [60] freeze out 4d orbitals, and are thus not directly suitable. There do exist plane-wave based, norm-conserving pseudopotentials that do keep those 4d electrons (and also optionally the 4s and 4p) explicitly [61]. At the same time, there is an indication that electron dynamics and spectra can be calculated with high accuracy using such semi-core pseudopotentials, as evidenced by a recent benchmark of computing L-edge XANES for Al<sub>2</sub>O<sub>3</sub> with 2s and 2p aluminum semi-core orbitals using TDDFT [62]. While this is not precisely the calculation we intend to run, this is a strong signal that carefully chosen pseudopotentials that include semi-core orbitals allow accurate calculation of dynamical properties like spectra, while freezing out deep core electrons and thus allowing to reduce the algorithmic cost.

The analysis above suggests that 4d semicore pseudopotentials for iodine exist. Unfortunately, that particular type of pseudopotential is not analytic, but fully numerical – the values of the pseudopotential and pseudowavefunctions are tabulated at each spatial point rather than expressed in terms of an analytical form. Since all the existing methods for implementing pseudopotentials in quantum algorithms rely on having an analytic form, this presents a further challenge to our resource reduction estimation process.

We approach this in the following way: we combine the widespread existence of analytic pseudopotentials [60], together with the evidence above about the existence of a high-quality numerical pseudopotential with 4d semicore inclusion [61], to assume that an analytic-style pseudopotential of good-enough quality with suitable inclusion of 4d may be constructed. As a stand-in for such a pseudopotential, we use the coefficients obtained in Ref. [60] for the key elements in the IMePh molecule: for the case of iodine, we consider the coefficients as given in the table in the reference, assuming that the only changes expected from the semicore 4d are the additional valence electrons – for a total of 17 – and perhaps some minor modification of the projector coefficients, to which the resource estimation is only weakly sensitive.

With this assumption, we turn to the pseudopotential implementation method described in Ref. [63] and specifically to the accompanying public Github repository <https://github.com/XanaduAI/pseudopotentials> for estimating the resource reduction.

We need one final assumption to make the estimates. The method of Ref. [63] only implements a single projector per angular momentum direction. For the IMePh system, based on the coefficients given in Ref. [60], all the elements include only a single projector per angular momentum except iodine: we assume that the cost of the block-encoding will not be significantly affected by this, which is expected from the literature.

With these assumptions in place, we can directly leverage the parameters of the IMePh system studied here – the unit cell size, chemical content, number of valence electrons of each constituent element, the projector coefficients – to make the estimates using the code in <https://github.com/XanaduAI/pseudopotentials>. These estimates are presented in the main text.